First-principles Calculation of Magnetism in Graphene Nanoribbons

Keisuke Sawada

January 10, 2012

Dissertation

First-principles Calculation of Magnetism in Graphene Nanoribbons

Graduate School of Natural Science & Technology
Kanazawa University

Major subject: Division of Mathematical and Physical Sciences

Course: Computational Science

School registration No. 0923102001

Name: Keisuke Sawada

Chief advisor: Mineo Saito

Abstract

There are two types of GNRs; one is the zigzag GNR (ZGNR) and the other is the armchair GNR (AGNR). ZGNRs have attracted scientific interests since the magnetic properties of graphenes are expected to originate from the edge states. Fujita et al. clarified that hydrogenated ZGNRs have flat electron bands. It is known that the freestanding ZGNR has the antiferromagnetic (AFM) ground state. On the other hand, the AGNRs are considered to have nonmagnetic (NM) properties.

In this study, I theoretically demonstrate that the finite magnetization is achieved in GNRs. I perform first-principles calculations of the ZGNR on Ni(111) substrate and dehydrogenated AGNR. I study the effect of the Ni(111) substrate on the magnetism of the ZGNR and the effect of the carrier doping on the magnetism of the dehydrogenated AGNR. I find that ZGNRs directly adsorbed on Ni(111) do not show flat-band ferromagnetism due to strong orbital hybridization between edge-localized C p-orbitals and Ni d-orbitals. The flat-band ferromagnetism of the ZGNR is recovered by introduction of a graphene sheet between the ZGNR and Ni(111) as a buffer layer which weakened the orbital hybridization. In this case, a parallel configuration of spin moments at the two edges has lower energy than the anti-parallel spin configuration whereas the magnetic ground state of the freestanding ZGNR has an antiparallel spin configuration. I explore the effects of orbital hybridization and charge transfer on the magnetic stability of ZGNRs on graphene/Ni(111).

I find that electron doping leads to magnetism in dehydrogenated AGNRs. In the case of field effect transistor doping, some amount of carriers injected into indirect-gap AGNRs induces halfmetallicity and heavily doped direct-gap AGNRs are AFM. I also find that N-doping induces

ferromagnetic insulators and half metals.

I clarify that the magnetism in the ZGNR is controlled by the orbital hybridization and charge transfer in ZGNRs on graphene/Ni(111). I find that the NM dehydrogenated AGNR is magnetized and becomes half-metal by electron doping. These findings open new possibility of carbon materials in the spintronics application.

Contents

Abstract **1**

1 Introduction **5**

1.1 Carbon materials 5

1.2 Zigzag graphene nanoribbon 5

1.3 Graphene on substrates 8

1.4 Armchair graphene nanoribbon 8

1.5 Aim of this work 8

1.6 Structure of this thesis 9

2 First-principles method **11**

2.1 Density functional theory 12

2.2 Exchange-correlation energy 15

2.3 Pseudopotential method 16

2.4 Linear combination of localized pseudoatomic orbitals method 18

2.5 Total energy 18

2.6 Charge analysis 24

2.6.1 Mulliken population 24

2.6.2 Voronoi Charge 25

3 Zigzag graphene nanoribbons on Ni(111) **27**

3.1 Monolayer zigzag graphene nanoribbon on Ni(111) 28

3.2 Graphene on Ni(111) 32
3.3 ZGNR/Graphene on Ni(111) 32
3.4 Conclusion 36

4 Dehydrogenated armchair graphene nanoribbon 37
4.1 Nondoped dehydrogenated AGNR 38
4.2 Electron-doped dehydrogenated AGNR 41
4.3 Nitrogen-doped dehydrogenated AGNR 46
4.4 Conclusion 49

5 Summary 50
5.1 Conclusion 50
5.2 Future plan 51

A Equilibrium Green's function method 53
A.1 Green's function 53
A.2 Self-Energy and Transmission 55
A.3 Noncollinear spin transmission 56
A.4 Test calculation: Zigzag graphene nanoribbon 57

References 60

Acknowledgments 64

Chapter 1

Introduction

1.1 Carbon materials

Carbon materials have various atomic structures (fullerenes, nanotubes, and graphenes as shown in Fig. 1.1). They attract much attention as candidates for the future development of the nano technology due to the light weight, high strength, and useful properties of semiconductors[1], metals[1], half metals[2, 3, 4], superconductors[5, 6] and magnets[7, 8, 9]. Graphene-based systems are ardently studied by successful fabrication of graphenes[10]. Among a variety of applications of graphenes, nano-scale spintronics applications are considered to be hopeful. For an example, spin transport has been experimentally observed by using single and multi graphene layers[11, 12, 13]. Recently, the field effect transistor (FET) used the graphene system is designed and the spin filter effect is theoretically predicted[14, 15]. Two years ago, the Nobel Prize in Physics for 2010 was awarded to A. Geim and K. Novoselov "for groundbreaking experiments regarding the two-dimensional material graphene".

1.2 Zigzag graphene nanoribbon

Graphene nanoribbon (GNR) is one of carbon materials. There are two types of GNRs; one is the zigzag GNR (ZGNR) and the other is the armchair GNR (AGNR) as shown in Fig. 1.2.

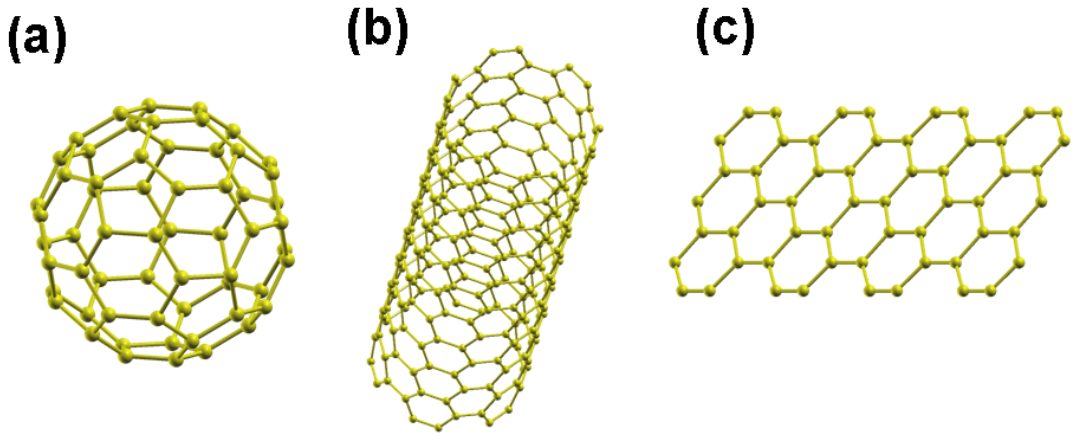

Figure 1.1: Carbon materials, (a) fullerenes, (b) nanotubes, (c) graphene

It was recently reported that graphene nanoribbons are experimentally synthesized from carbon nanotubes[16, 17]. ZGNRs are important in spintronics application because ZGNRs shows *flat-band ferromagnetism* induced by peculiar localized electronic states at each edge[8, 18]. Previous first-principles calculations predicted that the magnetic ground state of the ZGNR is an anti-parallel interedge spin (APIES) state: two ferromagnetic (FM) chains at the edges have opposite spin directions[19]. The cancellation of FM spin moment at each edge leads to the *zero* total magnetization of ZGNR. This antiferromagnetic (AFM) property originates from the cancellations of magnetic moments at the two sublattices in the honeycomb structure of the ZGNR. Since atoms at different edges belong to different sublattices, an antiparallel spin configuration at the two edges always appears. The cancellation of spin is supported by a theorem based on the Hubbard model under some conditions[20], i.e. according to this theorem, the total spin moment is given by $(N_{\mathrm{A}} - N_{\mathrm{B}})/2$, where N_{A} and N_{B} are the numbers of sublattices A and B, respectively. This theorem strongly supports the APIES state, but substantial total magnetization of ZGNR is expected to open a gateway into a spintronics application. So,

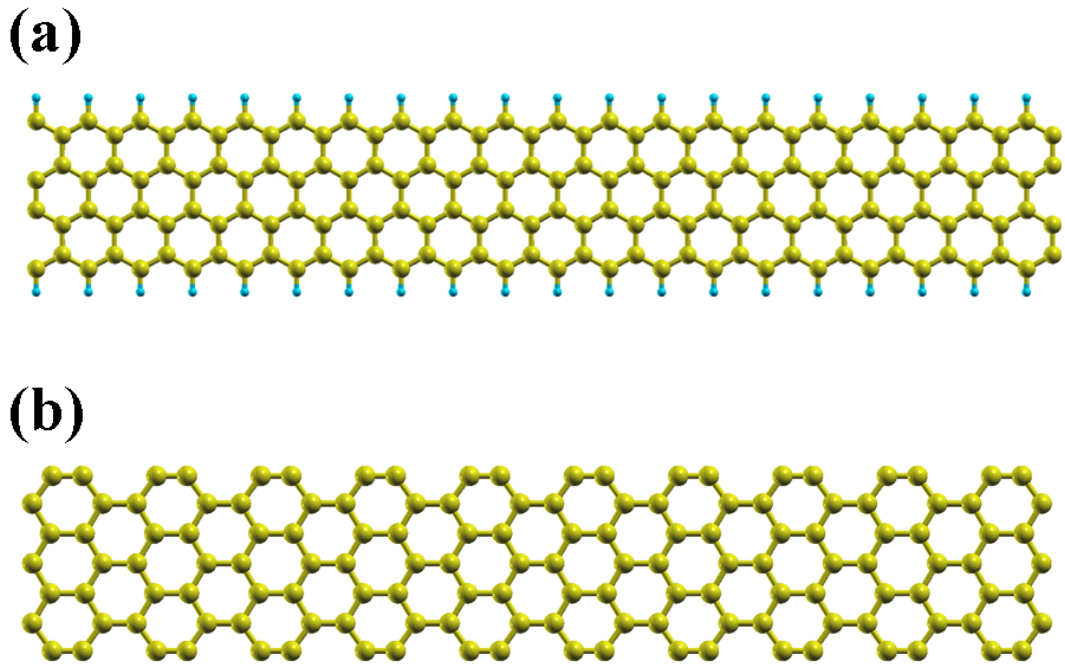

Figure 1.2: Lattice structure of (a) ZGNR and (b) dehydrogenated AGNR. The large and small spheres denote C and H atoms, respectively.

there were several attempts to obtain finite magnetization in ZGNRs. It was predicted that the ZGNR is magnetized when the numbers of monohydrogenated and dihydrogenated carbons are different[21]. In a previous study[22], I found that the magnetization of ZGNRs can be achieved by carrier doping. I also found that the spin canting angle θ defined as the relative angle between the magnetic moments at the two edges decreased monotonically from 180 to 0° with increasing carrier density. Therefore, both the novel canted interedge spin state and the parallel interedge spin (PIES) state were achieved, which indicates that the net magnetization of the ZGNR was obtained. I demonstrated that carrier injection could be carried out by either FET doping or chemical doping, suggesting that it is practically possible to control the magnetic phase.

1.3 Graphene on substrates

As noted above, it is previously reported that the ZGNR has the great potential for the spintronics application. So far, magnetism of freestanding systems of the monolayer type[8, 18, 19, 21, 22] and of multilayer types[23, 24, 25, 26, 27] have been mainly studied in ZGNRs. Since nano-devices are structured on substrates in practical applications, understanding of effects of substrates on magnetic properties of ZGNRs is necessary. The structural and electronic properties of graphene on substrates, such as Ni(111)[28], Co(0001)[29], Ru(0001)[30], Ir(111)[31], SiC[32] and SiO_2[33] were reported. Among them, the Ni(111) substrate is important because of the lattice commensuration[34]. Since the Ni substrate has a FM property, magnetism of ZGNRs is expected to be affected by the magnetic interaction between the substrate and ZGNRs. It is also noticed that there is charge transfer from metal substrate to the graphene[35]. It is expected that the magnetic state is also affected by this charge transfer.

1.4 Armchair graphene nanoribbon

AGNRs are energetically more stable than the ZGNR[36] and thus are offten observed than the zigzag edge in the edge of graphene experimentally[37]. The AGNR was believed to have the nonmagnetic (NM) structure whereas the magnetic properties due to the flat-band ferromagnetism in ZGNR attracted much attention. Recently, it was theoretically considered that *heavily doped hydrogenated* AGNRs have the FM ground state[38].

1.5 Aim of this work

Graphene-based materials attract much attention as candidates for the spintronics application. In particular, ZGNRs have the interest magnetic property originating from the flat-band ferromagnetism. In the freestanding ZGNR, the net magnetization is achieved by carrier doping whereas the magnetic ground state is the AFM insulator with no magnetization in the non-doped case. As carriers increase the magnetic state is changed from the APIES to the PIES state through

the noncollinear interedge spin state. If nano-devices are structured on substrates in practical applications, understanding relation between the ZGNR and substrate is important. Moreover, it is expected that the magnetic state can be controlled by carrier doping by the charge transfer from the substrate. On the other hand, the AGNR dose not have magnetic property. However, it is possible that the AGNR is also magnetized by carrier doping as well as the ZGNR case.

In this study, by using first-principles calculations, I estimate the potential of GNRs as the spintronics device. I clarify the magnetism in the monolayer ZGNR on Ni(111), the ZGNR on a graphene sheet over Ni(111) [ZGNR/graphene on Ni(111)], and carrier-induced dehydrogenated AGNRs. If the graphitic system can be available as the spintronics device, it is expected that the integration of the device used graphitic system is much higher than that of the traditional device. For example, there are the small transistor with the spin current or extremely small magnetic sensor etc. It is important for the spintronics application to predict the magnetic state by the first-principles calculation in nano-scale materials. However, it is experimentally difficult to particularly investigate the magnetic state in nano-scale materials. Therefore, this work is very significant.

1.6 Structure of this thesis

In this thesis, the calculation methods are explained in the Chapter 2. In the Chapter 3, the electronic and magnetic properties of ZGNRs on Ni(111) are shown. The magnetic moments of edges in the monolayer ZGNR on Ni(111) are very small and do not show *flat-band ferromagnetism*. On the other hand, it is found that the magnetic moments of edges are substantial in the case of the ZGNR/graphene on Ni(111). The magnitude of the moment is comparable with that in the free-standing case. The PIES state is the most stable and the direction of the magnetic moment of the ZGNR is parallel to that of the substrate. In the Chapter 4, the electronic and magnetic properties of dehydrogenated AGNRs are shown. Strong bonds are formed at the edges; thus, the electronic structure of the dehydrogenated AGNR is different from that of the hydrogenated AGNR. I find that the magnetic state of AGNRs is stable in a *wide range of*

electron doping. This magnetism originates from conduction bands having σ characters. In the case of field effect transistor doping, some of the electrons injected into indirect-gap AGNRs induce half-metallicity and heavily doped direct-gap AGNRs are AFM. I also find that N doping leads to FM properties. Finally, I summarize this work in Chapter 5.

Chapter 2

First-principles method

This work is studied by the first-principles calculation. The first-principles calculation is a non-empirical simulation method by using computers. The physical quantity is obtained by solving the quantum mechanical equation such as the Schrödinger equation. By using the first-principles calculation, I can understand the property under the extreme condition as the very high temperature and high pressure. Moreover, I can predict the property of the matter not existing in nature and design new materials. Therefore, the theoretical analysis of the electronic and magnetic structures by using the first-principles calculation is very effective in terms of the nano device application.

In this Chapter, I explain first-principles-calculatuion methods by consulting references[39, 40, 41, 42, 43]. I use the OpenMX calculation code. The OpenMX is based on density functional theories (DFT), the norm-conserving pseudopotentials, and local pseudo-atomic basis functions. I explain the density functional theory in section 2.1. In secction 2.2, the exchange-correlation energy is denoted. The pseudopotential and linear combination of localized pseudoatomic orbitals methods are described in section 2.2 and 2.3, respectively. I explain the total energy and charge analysis within the OpenMX in section 2.4 and 2.5, respectively.

2.1 Density functional theory

In this section, the DFT for electronic structures is described. DFT presents a powerful method for the calculation of the total energy and other observables of a many-electron systems. First, I consider the isolated *N* body.

$$H = T + V_{ee} + V_{ext} \tag{2.1}$$

$$\begin{cases} T = \sum_i -\frac{1}{2}\nabla_i^2 \\ V_{\mathrm{ee}} = \sum_{i<j} \frac{1}{|\mathbf{r}_i - \mathbf{r}_j|} \\ V_{\mathrm{ext}} = \sum_i v(\mathbf{r}_i) \end{cases} \tag{2.2}$$

where the H is the Hamiltonian, *T* is the kinetic energy, V_{ee} is the Coulomb potential between the electron and electron, V_{ext} is the external potential. $v(\mathbf{r})$ is the one-body Coulomb potential of the atomic nucleus. Thus, the electronic structure is analyzed for fixed nuclear positions (i.e. in the Born-Oppenheimer approximation).

The *N*-body Schrödinger equation is expressed as

$$H\Psi = E_0\Psi \tag{2.3}$$

where E_0 is the nondegenerate energy of the ground state, the Ψ is wavefunction. The E_0 is based on the variational principle and difined as

$$E_0[\Psi] = \min_{\Phi\to\Psi} \langle \Phi | H | \Phi \rangle \quad (\langle \Phi|\Phi\rangle = 1) \tag{2.4}$$

The Φ is represented by the linear combination of Slater determinant composed of the orthonormal basis function. The Ψ is determined by the variation of its coefficient. Ψ and E_0 are the functional of the external potential $v(\mathbf{r})$ i.e. $\Psi = \Psi[v], E_0 = E_0[v]$. Thus, it is possible to consider the external potential for all physical condition of the system.

The electronic density $\rho(\mathbf{r})$ is expressed as

$$\rho(\mathbf{r}) = N \int \Psi^*(x, x_2, \cdots, x_N)\, \Psi(x, x_2, \cdots, x_N)\, dx_2 dx_3 \cdots dx_N \quad (dx = d\mathbf{r}ds) \tag{2.5}$$

and the functional of the v. The fundamental of the DFT is one-on-one relation between the v and ρ. In addition, the inverse proposition is also satisfied in the case of the nondegenerate

energy of the ground state. Thus, the E_0 is the functional of the electronic density $\rho(\mathbf{r})$ and uniquely determined. In the nondegenerate ground state, v is determined as unique functional, Ψ is determined by the equation (2.4).

$$\rho(\mathbf{r}) \;\rightarrow\; v(\mathbf{r}) \;\rightarrow\; \Psi[\rho]$$

The physical quantity A is the functional of the ρ and expressed as

$$A[\rho] = \left\langle \Psi[\rho] \left| \hat{A} \right| \Psi[\rho] \right\rangle . \tag{2.6}$$

The energy E_0 is also the functional of ρ.

The $F[\rho(\mathbf{r})]$ is defined as the summation of the kinetic energy *T* and electron-electron interaction V_{ee}. Thus, the energy E_0 is

$$E_0[\rho(\mathbf{r})] = \int \rho(\mathbf{r}) v(\mathbf{r}) d\mathbf{r} + F[\rho(\mathbf{r})]. \tag{2.7}$$

$F[\rho(\mathbf{r})]$ is the functional determined by the only $\rho(\mathbf{r})$ and provided by the Ψ

$$F[\rho] = \min_{\Psi \rightarrow \rho} \langle \Psi[\rho] \left| T + V_{ee} \right| \Psi[\rho] \rangle . \tag{2.8}$$

Therefore, $F[\rho]$ is not depend on the v and obtained by the variational of the Ψ what gives ρ. The energy of the ground state is given by the minimization of the $E_0[\rho]$ and expressed as

$$\begin{aligned} E_0 &= \min_{\rho} E_0[\rho] \\ &= \min_{\rho} \left\{ \min_{\Psi \rightarrow \rho} \left[\langle \Psi[\rho] \left| T + V_{ee} \right| \Psi[\rho] \rangle + \int \rho(\mathbf{r}) v(\mathbf{r}) d\mathbf{r} \right] \right\} . \end{aligned} \tag{2.9}$$

If the functional $F[\rho(\mathbf{r})]$ is known, the energy of the ground state is simply obtained by the electronic density $\rho(\mathbf{r})$. Alothough this theorem is excat, the total energy is not known explicitly. So the $F[\rho]$ is expressed as

$$F[\rho] = T_{\mathrm{s}}[\rho] + \frac{1}{2} \iint \frac{\rho(\mathbf{r}) \rho(\mathbf{r}')}{|\mathbf{r} - \mathbf{r}'|} d\mathbf{r} d\mathbf{r}' + E_{\mathrm{ex}}[\rho]. \tag{2.10}$$

where the first term is the kinetic energy of the graound state in the independent-particle system without interactions, the second term is the the Coulomb interaction between the electron and

electron, the third term is exchange-correlation energy. To obtain the effective one-electron potential, the many-electron problem reduces to the one-electron problem by introducing the $T_{\rm s}[\rho]$. The system without interactions gives the $\rho(\mathbf{r})$ under the effective one-electron potential $v_{\rm eff}(\mathbf{r})$.

$$\left\{-\frac{1}{2}\nabla^2 + v_{\rm eff}(\mathbf{r})\right\}\psi_i(\mathbf{r}) = \epsilon_i\psi_i(\mathbf{r}) \tag{2.11}$$

$$\rho(\mathbf{r}) = \sum_i |\psi_i(\mathbf{r})|^2 \tag{2.12}$$

where the summation of *i* is performed for only the number of electrons in ascending order of the ϵ_i and taken account of the freedom degree of the spin state. $v_{\rm eff}(\mathbf{r})$ is expressed as

$$v_{\rm eff}(\mathbf{r}) = v(\mathbf{r}) + \int \frac{\rho(\mathbf{r}')}{|\mathbf{r}-\mathbf{r}'|}d\mathbf{r}' + v_{\rm xc}[\rho(\mathbf{r})] \tag{2.13}$$

$$v_{\rm xc}[\rho(\mathbf{r})] = \frac{\delta E_{\rm ex}[\rho]}{\delta\rho(\mathbf{r})}. \tag{2.14}$$

Meanwhile, the total energy of the independent-particle system (the summation of the one-electron energy) is expressed as

$$E_{\rm s}[\rho] = T_{\rm s}[\rho] + \int \rho(\mathbf{r})v_{\rm s}(\mathbf{r})d\mathbf{r} \tag{2.15}$$

If the virtual independent-particle system has the same ground state as the real interacting system, the many-electron problem reduces to the one-electron problem. Thus,

$$v_{\rm s}(\mathbf{r}) = v_{\rm eff}(\mathbf{r}). \tag{2.16}$$

The kinetic energy $T_{\rm s}$ is expressed as

$$T_{\rm s}[\rho] = \sum_i \epsilon_i - \int \rho(\mathbf{r})v_{\rm eff}(\mathbf{r})d\mathbf{r}. \tag{2.17}$$

By substituting this formula into the equation (2.10), the total energy is obtained as follows:

$$E[\rho(\mathbf{r})] = \sum_i \epsilon_i + \frac{1}{2}\iint \frac{\rho(\mathbf{r})\rho(\mathbf{r}')}{|\mathbf{r}-\mathbf{r}'|}d\mathbf{r}d\mathbf{r}' + E_{\rm ex}[\rho] - \int \rho(\mathbf{r})v_{\rm eff}(\mathbf{r})d\mathbf{r}. \tag{2.18}$$

The equations (2.11),(2.12),(2.13),and (2.14) is called Kohn-Sham equation. The Kohn-Sham equation is solved by the self-consistent scheme as shown in Fig. 2.1.

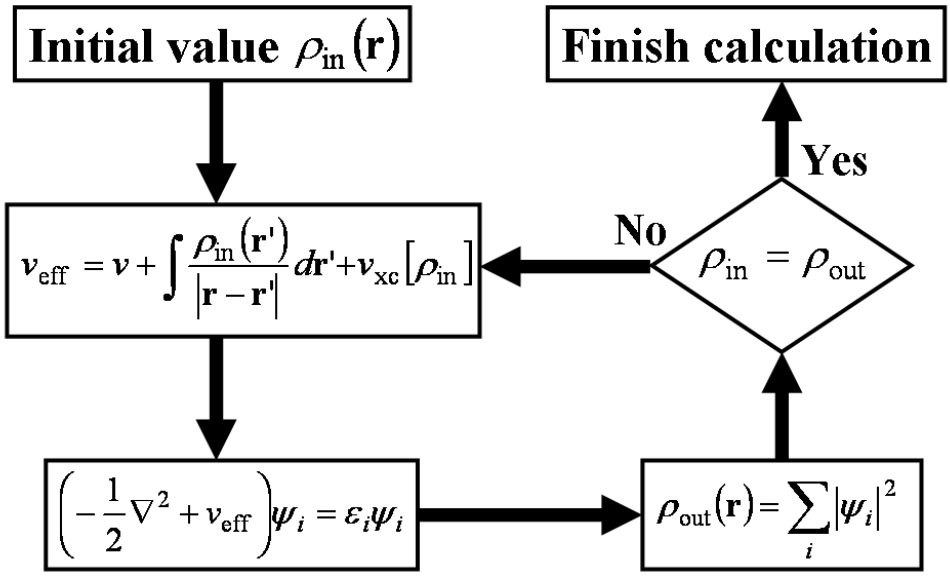

Figure 2.1: Self-consistent scheme of Kohn-Sham equation

2.2 Exchange-correlation energy

In the previous section, the many body problem is rewritten to the effective one-electron problem by using the Kohn-Sham equation. But, the Kohn-Sham equation can not be solved since the derivation of $E_{\text{xc}}[\rho]$ i.e. $v_{xc} = \delta E_{\text{xc}}[\rho]/\delta\rho(\mathbf{r})$ is not known. Here, the functional of $E_{\text{xc}}[\rho]$ is formed by approximating $E_{\text{xc}}[\rho]$ by the local homogeneous electron gas model. Fortunately, this can be approximated well by a functional of the form

$$E_{\text{xc}}[\rho] = \int \rho(\mathbf{r})\epsilon_{\text{xc}}\left(\rho(\mathbf{r})\right) d\mathbf{r} \tag{2.19}$$

where $\epsilon_{\text{xc}}\left(\rho(\mathbf{r})\right)$ is exchange-correlation-enegy density. This approximation is called the local density approximation (LDA). $E_{\text{xc}}[\rho]$ in the spin polarized case is called the local spin density approximation (LSDA) and expressed as

$$E_{\text{xc}}[\rho_\uparrow, \rho_\downarrow] = \int \rho(\mathbf{r})\epsilon_{\text{xc}}\left(\rho_\uparrow(\mathbf{r}), \rho_\downarrow(\mathbf{r})\right) d\mathbf{r}. \tag{2.20}$$

However, the electronic density is inhomogeneous in the real system, so some limitations apply to the LDA. For example, the band gap is underestimated by the LDA. One of the breakthrough for the problem of the LDA is the generalized gradient approximation (GGA)[40]. To accurately treat the space variation of the electronic density, the derivation of $\rho(\mathbf{r})$ for $\mathbf{r}$ is considered. The functional of the GGA is written by

$$E_{\mathrm{xc}}[\rho_\uparrow, \rho_\downarrow] = \int f\left(\rho_\uparrow(\mathbf{r}), \rho_\downarrow(\mathbf{r}), \nabla\rho_\uparrow(\mathbf{r}), \nabla\rho_\downarrow(\mathbf{r})\right) d\mathbf{r}. \tag{2.21}$$

2.3 Pseudopotential method

The pseudopotential method treats the motion of valence electron in the made weak Coulomb field by assembling the core electron and atomic nucleus. However, the core electron weaken the effect of the positive charge of the atomic nucleus and has the kinetic energy. The potential introduced this effect is coupled with the DFT within the LDA and built the method of constructing the non-empirical pseudopotential. This potential is called the norm-conserving pseudopotential. When the Kohn-Sham equation within the LDA is solved in the isolated atom, the coordinates of the electronic wavefunction is transformed to the polar coordinate with the origin of atomic nucleus. The angular variables are given by the spherical surface harmonics Y_{lm} and separated, thus the radial part is only considered as

$$\left[-\frac{\hbar^2}{2m}\frac{d^2}{dr^2} + \frac{\hbar^2 l(l+1)}{2mr^2} + V(r)\right] rR_l(r;\epsilon) = \epsilon_l rR_l(r;\epsilon). \tag{2.22}$$

where the $V(r)$ is all potentials which interacts the electrons. This equation is represented by using the atomic units and the operator

$$D_l = -\frac{1}{2}\frac{d^2}{dr^2} + \frac{l(l+1)}{2r^2} \tag{2.23}$$

and $W_l(r) = rR_l(r)$ are used. The equation (2.22) is rewritten by

$$\left[D_l + V(r)\right] W_l(r) = \epsilon_l W_l(r). \tag{2.24}$$

The radial function is normalized as follows:

$$\int_0^\infty \left[rR_l(r)\right]^2 dr = \int_0^\infty \left[W_l(r)\right]^2 dr = 1. \tag{2.25}$$

First, I solve the self-consistent Koh-Sham equation within the LDA in the isolated atom and make the potential of all electrons $V(r)$. The $V(r)$ is consist of the Coulomb-attraction field of the atomic nucleus $(-Ze/r)$, the Coulomb repulsion between the electron and electron, and the exchange-correlation potential. I make the norm-conserving pseudopotential which interacts the valence electron to satisfy the following four conditions.

1. The bottommost energy eigenvalue for the pseudopotential is consistent with the energy eigenvalue of the valence electron obtained by the all-electron calculation.

2. In the region of $r > r_c$ with respect to a certain core radius r_c, the true wavefunction $R_l^{\rm t}(r)$ derived from the $V(r)$ of the atomic nucleus is consistent with pseudo-wavefunction $R_l^{\rm ps}(r)$ derived from the pseudopotential.

3. The following norm-conserving

$$\int_0^{r_c} \left[rR_l^{\rm ps}(r)\right]^2 dr = \int_0^{r_c} \left[rR_l^{\rm t}(r)\right]^2 dr \tag{2.26}$$

   is satisfied.

The condition 1 means that the pseudopotential affected from the valence electron is equivalent to the potential $V(r)$ obtained by the all-electron calculation. The condition 2 is natural in the region of $r > r_c$ with respect to a certain core radius r_c. The square of the wavefunction is the charge. The condition 3 means that the all charge of the pseudopotential is equivalent to that of the true potential in the region of $r < r_c$ and the electrostatic potential which affects to the valence electron is unchanged by the Gauss theorem in the region of $r > r_c$. Moreover, the following condition is derived from the conditions 2 and 3.

4. The logarithmic derivative of the pseudo-wavefunction $R_l^{\rm ps}(r)$ in the $r = r_c$ and derivative for the energy of the logarithmic derivative ϵ are consistent with the those corresponding to the $R_l^{\rm t}(r)$.

According to the scatter theory, if the logarithmic derivative of the wavefunction in the $r = r_c$ is equal, the scattering wave of the pseudopotential is perfectly consistent with that of

the true potential in the region of $r > r_c$. Therefore, the phase shifting of the scattering wave given by both potentials fits. Moreover, when the first derivation for the ϵ is equal, the energy eigenvalue changes to the $\epsilon + \Delta\epsilon$ by changing the potential. Even if it affects the scattering wave, its effect is treated till the first order of the $\Delta\epsilon$. The change of the potential means that the potential $V(r)$ changes in the molecule or atoms of the solid. Even if the environment changes, the pseudopotential which produce a good result is called that the *transferability* is good.

2.4 Linear combination of localized pseudoatomic orbitals method

The linear combination of localized pseudoatomic orbitals (LCPAO) method is represented by the linear combination of atomic orbitals. By using the numerical atomic orbital $\phi_{i\alpha}$, the Kohn-Sham orbital ψ_μ is expanded as

$$\psi_\mu(\mathbf{r}) = \sum_{i\alpha} c_{\mu,i\alpha}\phi_{i\alpha}(\mathbf{r} - \mathbf{r}_i). \tag{2.27}$$

where *i* is the site index, $\alpha \equiv (plm)$ is the organized orbital index, and $\phi_{i\alpha} \equiv Y_{lm}R_{iplm}$. A radial wave function R_{ipl} depends on not only an angular momentum quantum number *l*, but also a site index *i*, and a multiplicity index *p*. Note that these argument is restricted within only nonspin-polarized systems and a non-Bloch expression of the one-particle wave functions for simplicity, but the extensions of these argument to those are straightforward. I can solve the following eigenvalue problem

$$\sum_{j\beta}\langle\phi_{i\alpha}\left|\hat{H}\right|\phi_{j\beta}\rangle c_{\mu,j\beta} = \epsilon_\mu \sum_{j\beta}\langle\phi_{i\alpha}|\phi_{j\beta}\rangle c_{\mu,j\beta}. \tag{2.28}$$

2.5 Total energy

In this and next sections, I describe the total energy and charge analysis for the spin-polarized system by consulting technical notes on OpenMX[43]. The Kohn-Sham Bloch functions ψ_μ are

expanded in a form of LCPAO $\phi_{i\alpha}$ centered on site τ_i by

$$\psi^{(\mathbf{k})}_{\sigma\mu}(\mathbf{r}) = \frac{1}{\sqrt{N}} \sum_{n}^{N} e^{i\mathbf{R}_n\cdot\mathbf{k}} \sum_{i\alpha} c^{(\mathbf{k})}_{\sigma\mu,i\alpha}\phi_{i\alpha}(\mathbf{r}-\tau_i-\mathbf{R}_n), \tag{2.29}$$

where *c* and ϕ are an expansion coefficient and pseudo-atomic function, $\mathbf{R}_n$ a lattice vector, *i* a site index, σ ($\uparrow$ and $\downarrow$) spin index, $\alpha \equiv (plm)$ an organized orbital index with a multiplicity index *p*, an angular momentum quantum number *l*, and a magnetic quantum number *m*. The charge density operator $\hat{n}_\sigma$ for the spin index σ is given by

$$\hat{n}_\sigma = \frac{1}{V_{\mathrm{B}}} \int_{\mathrm{B}} dk^3 \sum_{\mu}^{\mathrm{occ}} \left|\psi^{(\mathbf{k})}_{\sigma\mu}\right\rangle\left\langle\psi^{(\mathbf{k})}_{\sigma\mu}\right|, \tag{2.30}$$

where $\int_{\mathrm{B}}$ means the integration over the first Brillouin zone of which volume is V_{B}, and $\sum^{\mathrm{occ}}$ means the summation over occupied states. The charge density $n_\sigma(\mathbf{r})$ with the spin index σ is found as

$$\begin{aligned}
n_\sigma(\mathbf{r}) &= \langle\mathbf{r}\,|\hat{n}_\sigma|\,\mathbf{r}\rangle \\
&= \frac{1}{V_{\mathrm{B}}}\int_{\mathrm{B}} dk^3 \sum_{\mu}^{\mathrm{occ}} \langle\mathbf{r}\left|\psi^{(\mathbf{k})}_{\sigma\mu}\right\rangle\left\langle\psi^{(\mathbf{k})}_{\sigma\mu}\right|\mathbf{r}\rangle \\
&= \frac{1}{V_{\mathrm{B}}}\int_{\mathrm{B}} dk^3 \sum_{\mu}^{\mathrm{occ}} \langle\mathbf{r}\left|e^{-i\mathbf{R}_{n'}\cdot\mathbf{k}}\right|\psi^{(\mathbf{k})}_{\sigma\mu}(\mathbf{r}+\mathbf{R}_{n'})\rangle\langle\psi^{(\mathbf{k})}_{\sigma\mu}|\mathbf{r}\rangle \quad (\text{Bloch theory}) \\
&= \frac{1}{V_{\mathrm{B}}}\int_{\mathrm{B}} dk^3 \sum_{\mu}^{\mathrm{occ}} e^{-i\mathbf{R}_{n'}\cdot\mathbf{k}} \cdot \frac{1}{\sqrt{N}} \sum_{n'}^{N} e^{i\mathbf{R}_{n'}\cdot\mathbf{k}} \sum_{j\beta} c^{(\mathbf{k})}_{\sigma\mu,j\beta}\,\langle\mathbf{r}|\phi_{j\beta}(\mathbf{r}-\tau_j)\rangle \\
&\quad \cdot\frac{1}{\sqrt{N}} \sum_{n}^{N} e^{i\mathbf{R}_n\cdot\mathbf{k}} \sum_{i\alpha} c^{(\mathbf{k})*}_{\sigma\mu,i\alpha}\,\langle\phi_{i\alpha}(\mathbf{r}-\tau_i-\mathbf{R}_n)|\mathbf{r}\rangle \\
&= \frac{1}{V_{\mathrm{B}}}\int_{\mathrm{B}} dk^3 \sum_{n}^{N}\sum_{i\alpha,j\beta}\sum_{\mu}^{\mathrm{occ}} e^{i\mathbf{R}_n\cdot\mathbf{k}} c^{(\mathbf{k})*}_{\sigma\mu,i\alpha} c^{(\mathbf{k})}_{\sigma\mu,j\beta}\phi_{j\beta}(\mathbf{r}-\tau_j)\phi^*_{i\alpha}(\mathbf{r}-\tau_i-\mathbf{R}_n) \\
&= \sum_{n}^{N}\sum_{i\alpha,j\beta} \rho^{(\mathbf{R}_n)}_{\sigma,i\alpha,j\beta}\phi_{j\beta}(\mathbf{r}-\tau_j)\phi^*_{i\alpha}(\mathbf{r}-\tau_i-\mathbf{R}_n)
\end{aligned} \tag{2.31}$$

with a density matrix defined by

$$\rho^{(\mathbf{R}_n)}_{\sigma,i\alpha,j\beta} = \frac{1}{V_{\mathrm{B}}}\int_{\mathrm{B}} dk^3 \sum_{\mu}^{\mathrm{occ}} e^{i\mathbf{R}_n\cdot\mathbf{k}} c^{(\mathbf{k})*}_{\sigma\mu,i\alpha} c^{(\mathbf{k})}_{\sigma\mu,j\beta}. \tag{2.32}$$

Although it is assumed that the electronic temperature is zero in this notes, OpenMX uses the Fermi-Dirac function with a finite temperature in the practical implementation. Therefore, the force on atom becomes inaccurate for metallic systems or very high temperature. The total charge density *n* is the sum of $n_\uparrow$ and $n_\downarrow$ as follows:

$$n(\mathbf{r}) = n_\uparrow(\mathbf{r}) + n_\downarrow(\mathbf{r}). \tag{2.33}$$

Also, it is convenient to define a difference charge density $\delta n(\mathbf{r})$ for later discussion as

$$\begin{aligned} \delta n(\mathbf{r}) &= n(\mathbf{r}) - n^{(a)}(\mathbf{r}) \\ &= n(\mathbf{r}) - \sum_i n_i^{(a)}(\mathbf{r}) \end{aligned} \tag{2.34}$$

where $n_i^{(a)}$ is an atomic charge density evaluated by a confinement atomic calculations associated with the site *i*. Within the local density approximation (LDA) and generalized gradient approximation (GGA), the total energy of the collinear case is given by the sum of the kinetic energy $E_{\rm kin}$, the electron-core Coulomb energy $E_{\rm ec}$, the electron-electron Coulomb energy $E_{\rm ee}$, the exchange-correlation energy $E_{\rm xc}$, and the core-core Coulomb energy $E_{\rm cc}$ as

$$E_{\rm tot} = E_{\rm kin} + E_{\rm ec} + E_{\rm ee} + E_{\rm xc} + E_{\rm cc}. \tag{2.35}$$

The kinetic energy $E_{\rm kin}$ is given by

$$\begin{aligned} E_{\rm kin} &= \frac{1}{V_{\rm B}} \int_{\rm B} dk^3 \sum_\sigma \sum_\mu^{\rm occ} \left\langle \psi_{\sigma\mu}^{(\mathbf{k})} \left| \hat{T} \right| \psi_{\sigma\mu}^{(\mathbf{k})} \right\rangle \\ &= \frac{1}{V_{\rm B}} \int_{\rm B} dk^3 \sum_\sigma \sum_\mu^{\rm occ} \sum_n^N \sum_{i\alpha,j\beta} e^{i\mathbf{R}_n\cdot\mathbf{k}} c_{\sigma\mu,i\alpha}^{(\mathbf{k})*} c_{\sigma\mu,j\beta}^{(\mathbf{k})} \left\langle \phi_{i\alpha}(\mathbf{r}-\tau_i) \left| \hat{T} \right| \phi_{j\beta}(\mathbf{r}-\tau_j-\mathbf{R}_n) \right\rangle \\ &= \sum_\sigma \sum_n^N \sum_{i\alpha,j\beta} \rho_{\sigma,i\alpha,j\beta}^{(\mathbf{R}_n)} h_{i\alpha,j\beta,{\rm kin}}^{(\mathbf{R}_n)}. \end{aligned} \tag{2.36}$$

The electron-core Coulomb energy $E_{\rm ec}$ is given by two contributions $E_{\rm ec}^{\rm (L)}$ and $E_{\rm ec}^{\rm (NL)}$ related to the local and non-local parts of pseudopotentials:

$$
\begin{aligned}
E_{\rm ec} &= E_{\rm ec}^{\rm (L)} + E_{\rm ec}^{\rm (NL)} \\
&= \frac{1}{V_{\rm B}} \int_{\rm B} dk^3 \sum_{\sigma} \sum_{\mu}^{\rm occ} \left\langle \psi_{\sigma\mu}^{(\mathbf{k})} \middle| \sum_{I} \{ V_{{\rm core},I}(\mathbf{r}-\tau_I) + V_{{\rm NL},I}(\mathbf{r}-\tau_I) \} \middle| \psi_{\sigma\mu}^{(\mathbf{k})} \right\rangle \\
&= \frac{1}{V_{\rm B}} \int_{\rm B} dk^3 \sum_{\sigma} \sum_{\mu}^{\rm occ} \sum_{n}^{N} \sum_{i\alpha,j\beta} e^{i\mathbf{R}_n\cdot\mathbf{k}} c_{\sigma\mu,i\alpha}^{(\mathbf{k})*} c_{\sigma\mu,j\beta}^{(\mathbf{k})} \\
&\quad \cdot \left\langle \phi_{i\alpha}(\mathbf{r}-\tau_i) \middle| \sum_{I} V_{{\rm core},I}(\mathbf{r}-\tau_I) \middle| \phi_{j\beta}(\mathbf{r}-\tau_j-\mathbf{R}_n) \right\rangle \\
&\quad + \frac{1}{V_{\rm B}} \int_{\rm B} dk^3 \sum_{\sigma} \sum_{\mu}^{\rm occ} \sum_{n}^{N} \sum_{i\alpha,j\beta} e^{i\mathbf{R}_n\cdot\mathbf{k}} c_{\sigma\mu,i\alpha}^{(\mathbf{k})*} c_{\sigma\mu,j\beta}^{(\mathbf{k})} \\
&\quad \cdot \left\langle \phi_{i\alpha}(\mathbf{r}-\tau_i) \middle| \sum_{I} V_{{\rm NL},I}(\mathbf{r}-\tau_I) \middle| \phi_{j\beta}(\mathbf{r}-\tau_j-\mathbf{R}_n) \right\rangle \\
&= \sum_{\sigma} \sum_{n}^{N} \sum_{i\alpha,j\beta} \rho_{\sigma,i\alpha,j\beta}^{(\mathbf{R}_n)} \left\langle \phi_{i\alpha}(\mathbf{r}-\tau_i) \middle| \sum_{I} V_{{\rm core},I}(\mathbf{r}-\tau_I) \middle| \phi_{j\beta}(\mathbf{r}-\tau_j-\mathbf{R}_n) \right\rangle \\
&\quad + \sum_{\sigma} \sum_{n}^{N} \sum_{i\alpha,j\beta} \rho_{\sigma,i\alpha,j\beta}^{(\mathbf{R}_n)} \left\langle \phi_{i\alpha}(\mathbf{r}-\tau_i) \middle| \sum_{I} V_{{\rm NL},I}(\mathbf{r}-\tau_I) \middle| \phi_{j\beta}(\mathbf{r}-\tau_j-\mathbf{R}_n) \right\rangle
\end{aligned}
\tag{2.37}
$$

where $V_{{\rm core},I}$ and $V_{{\rm NL},I}$ are the local and non-local parts of pseudopotential located on a site *I*. Thus, I have

$$
\begin{aligned}
E_{\rm ec}^{\rm (L)} &= \sum_{\sigma} \sum_{n}^{N} \sum_{i\alpha,j\beta} \rho_{\sigma,i\alpha,j\beta}^{(\mathbf{R}_n)} \left\langle \phi_{i\alpha}(\mathbf{r}-\tau_i) \middle| \sum_{I} V_{{\rm core},I}(\mathbf{r}-\tau_I) \middle| \phi_{j\beta}(\mathbf{r}-\tau_j-\mathbf{R}_n) \right\rangle \\
&= \int dr^3 n(\mathbf{r}) \sum_{I} V_{{\rm core},I}(\mathbf{r}-\tau_I)
\end{aligned}
\tag{2.38}
$$

$$
E_{\rm ec}^{\rm (NL)} = \sum_{\sigma} \sum_{n}^{N} \sum_{i\alpha,j\beta} \rho_{\sigma,i\alpha,j\beta}^{(\mathbf{R}_n)} \left\langle \phi_{i\alpha}(\mathbf{r}-\tau_i) \middle| \sum_{I} V_{{\rm NL},I}(\mathbf{r}-\tau_I) \middle| \phi_{j\beta}(\mathbf{r}-\tau_j-\mathbf{R}_n) \right\rangle . \tag{2.39}
$$

The electron-electron Coulomb energy $E_{\rm ee}$ is given by

$$\begin{aligned} E_{\rm ee} &= \frac{1}{2}\iint dr^3 dr'^3 \frac{n(\mathbf{r})n(\mathbf{r}')}{|\mathbf{r}-\mathbf{r}'|} \\ &= \frac{1}{2}\int dr^3 n(\mathbf{r}) V_{\rm H}(\mathbf{r}) \\ &= \frac{1}{2}\int dr^3 n(\mathbf{r}) \left\{ V_{\rm H}^{(a)}(\mathbf{r}) + \delta V_{\rm H}(\mathbf{r}) \right\} \end{aligned} \tag{2.40}$$

where $V_{\rm H}$ is decomposed into two contributions $V_{\rm H}^{(a)}$ and $\delta V_{\rm H}(\mathbf{r})$ coming from the superposition of atomic charge densities and the difference charge density $\delta n(\mathbf{r})$ defined by

$$\begin{aligned} V_{\rm H}^{(a)}(\mathbf{r}) &= \sum_I \int dr'^3 \frac{n_I^{(a)}(\mathbf{r})}{|\mathbf{r}-\mathbf{r}'|} \\ &= \sum_I V_{{\rm H},I}^{(a)}(\mathbf{r}-\tau_I) \end{aligned} \tag{2.41}$$

$$\delta V_{\rm H}(\mathbf{r}) = \int dr'^3 \frac{\delta n(\mathbf{r})}{|\mathbf{r}-\mathbf{r}'|}. \tag{2.42}$$

Within the LDA, the exchange-correlation energy $E_{\rm xc}$ is given by

$$E_{\rm xc} = \int dr^3 \left\{ n_\uparrow(\mathbf{r}) + n_\downarrow(\mathbf{r}) + n_{\rm pcc}(\mathbf{r}) \right\} \epsilon_{\rm xc} \left(n_\uparrow + \frac{1}{2} n_{\rm pcc},\ n_\downarrow + \frac{1}{2} n_{\rm pcc} \right) \tag{2.43}$$

where $n_{\rm pcc}$ is a charge density used for a partial core correction (PCC). The core-core Coulomb energy $E_{\rm cc}$ is given as repulsive Coulomb interactions among effective core charge Z_I considered in the generation of pseudopotentials by

$$E_{\rm cc} = \frac{1}{2}\sum_{I,J} \frac{Z_I Z_J}{|\tau_I - \tau_J|}. \tag{2.44}$$

for numerical accuracy and efficiency it is important to reorganize the sum of three terms $E_{\rm ec}^{\rm (L)}$, $E_{\rm ee}$, and $E_{\rm cc}$, as follows:

$$
\begin{aligned}
E_{\rm ec}^{\rm (L)} + E_{\rm ee} + E_{\rm cc} &= \int dr^3 n(\mathbf{r}) \sum_I V_{{\rm core},I}(\mathbf{r}-\tau_I) + \int dr^3 n(\mathbf{r}) V_{\rm H}^{(a)}(\mathbf{r}) - \int dr^3 n(\mathbf{r}) V_{\rm H}^{(a)}(\mathbf{r}) \\
&\quad + \frac{1}{2}\int dr^3 n(\mathbf{r}) \left\{ V_{\rm H}^{(a)}(\mathbf{r}) + \delta V_{\rm H}(\mathbf{r}) \right\} + \frac{1}{2}\int dr^3 n^{(a)}(\mathbf{r}) V_{\rm H}^{(a)}(\mathbf{r}) \\
&\quad - \frac{1}{2}\int dr^3 n^{(a)}(\mathbf{r}) V_{\rm H}^{(a)}(\mathbf{r}) + \frac{1}{2}\sum_{I,J} \frac{Z_I Z_J}{|\tau_I - \tau_J|} \\
&= \int dr^3 n(\mathbf{r}) \sum_I V_{{\rm core},I}(\mathbf{r}-\tau_I) + \int dr^3 n(\mathbf{r}) \sum_I V_{{\rm H,I}}^{(a)}(\mathbf{r}-\tau_I) \\
&\quad - \int dr^3 n(\mathbf{r}) V_{\rm H}^{(a)}(\mathbf{r}) + \frac{1}{2}\int dr^3 n(\mathbf{r}) V_{\rm H}^{(a)}(\mathbf{r}) + \frac{1}{2}\int dr^3 n(\mathbf{r}) \delta V_{\rm H}(\mathbf{r}) \\
&\quad + \frac{1}{2}\int dr^3 n^{(a)}(\mathbf{r}) V_{\rm H}^{(a)}(\mathbf{r}) + \frac{1}{2}\sum_{I,J} \left\{ \frac{Z_I Z_J}{|\tau_I - \tau_J|} - \int dr^3 n_I^{(a)}(\mathbf{r}) V_{{\rm H},J}^{(a)}(\mathbf{r}-\tau_J) \right\} \\
&= \int dr^3 n(\mathbf{r}) \sum_I V_{{\rm na},I}(\mathbf{r}-\tau_I) + \frac{1}{2}\int dr^3 n(\mathbf{r}) \delta V_{\rm H}(\mathbf{r}) - \frac{1}{2}\int dr^3 n(\mathbf{r}) V_{\rm H}^{(a)}(\mathbf{r}) \\
&\quad + \frac{1}{2}\int dr^3 n^{(a)}(\mathbf{r}) V_{\rm H}^{(a)}(\mathbf{r}) + \frac{1}{2}\sum_{I,J} \left\{ \frac{Z_I Z_J}{|\tau_I - \tau_J|} - \int dr^3 n_I^{(a)}(\mathbf{r}) V_{{\rm H},J}^{(a)}(\mathbf{r}-\tau_J) \right\} \\
&= \int dr^3 n(\mathbf{r}) \sum_I V_{{\rm na},I}(\mathbf{r}-\tau_I) + \frac{1}{2}\int dr^3 n(\mathbf{r}) \delta V_{\rm H}(\mathbf{r}) - \frac{1}{2}\int dr^3 \delta n(\mathbf{r}) V_{\rm H}^{(a)}(\mathbf{r}) \\
&\quad + \frac{1}{2}\sum_{I,J} \left\{ \frac{Z_I Z_J}{|\tau_I - \tau_J|} - \int dr^3 n_I^{(a)}(\mathbf{r}) V_{{\rm H},J}^{(a)}(\mathbf{r}-\tau_J) \right\} \\
&= \int dr^3 n(\mathbf{r}) \sum_I V_{{\rm na},I}(\mathbf{r}-\tau_I) + \frac{1}{2}\int dr^3 \delta n(\mathbf{r}) \delta V_{\rm H}(\mathbf{r}) + \frac{1}{2}\int dr^3 n^{(a)}(\mathbf{r}) \delta V_{\rm H}(\mathbf{r}) \\
&\quad - \frac{1}{2}\int dr^3 \delta n(\mathbf{r}) V_{\rm H}^{(a)}(\mathbf{r}) + \frac{1}{2}\sum_{I,J} \left\{ \frac{Z_I Z_J}{|\tau_I - \tau_J|} - \int dr^3 n_I^{(a)}(\mathbf{r}) V_{{\rm H},J}^{(a)}(\mathbf{r}-\tau_J) \right\} \\
&= \int dr^3 n(\mathbf{r}) \sum_I V_{{\rm na},I}(\mathbf{r}-\tau_I) + \frac{1}{2}\int dr^3 \delta n(\mathbf{r}) \delta V_{\rm H}(\mathbf{r}) \\
&\quad + \frac{1}{2}\int dr^3 n^{(a)}(\mathbf{r}) \int dr'^3 \frac{\delta n(\mathbf{r})}{|\mathbf{r}-\mathbf{r}'|} - \frac{1}{2}\int dr^3 \delta n(\mathbf{r}) \int dr'^3 \frac{n^{(a)}(\mathbf{r})}{|\mathbf{r}-\mathbf{r}'|} \\
&\quad + \frac{1}{2}\sum_{I,J} \left\{ \frac{Z_I Z_J}{|\tau_I - \tau_J|} - \int dr^3 n_I^{(a)}(\mathbf{r}) V_{{\rm H},J}^{(a)}(\mathbf{r}-\tau_J) \right\} \\
&= \int dr^3 n(\mathbf{r}) \sum_I V_{{\rm na},I}(\mathbf{r}-\tau_I) + \frac{1}{2}\int dr^3 \delta n(\mathbf{r}) \delta V_{\rm H}(\mathbf{r}) \\
&\quad + \frac{1}{2}\sum_{I,J} \left\{ \frac{Z_I Z_J}{|\tau_I - \tau_J|} - \int dr^3 n_I^{(a)}(\mathbf{r}) V_{{\rm H},J}^{(a)}(\mathbf{r}-\tau_J) \right\} \qquad (2.45)
\end{aligned}
$$

where

$$V_{\mathrm{na},I}(\mathbf{r}-\tau_I) = V_{\mathrm{core},I}(\mathbf{r}-\tau_I) + V^{(a)}_{\mathrm{H},I}(\mathbf{r}-\tau_I). \tag{2.46}$$

Therefore, I can reorganize these three terms as follows:

$$E^{(\mathrm{L})}_{\mathrm{ec}} + E_{\mathrm{ee}} + E_{\mathrm{cc}} = E_{\mathrm{na}} + E_{\delta\mathrm{ee}} + E_{\mathrm{scc}} \tag{2.47}$$

$$\begin{aligned} E_{\mathrm{na}} &= \int dr^3 n(\mathbf{r}) \sum_I V_{\mathrm{na},I}(\mathbf{r}-\tau_I) \\ &= \sum_\sigma \sum_n^N \sum_{i\alpha,j\beta} \rho^{(\mathbf{R}_n)}_{\sigma,i\alpha,j\beta} \sum_I \langle \phi_{i\alpha}(\mathbf{r}-\tau_i) \left| V_{\mathrm{na},I}(\mathbf{r}-\tau_I) \right| \phi_{j\beta}(\mathbf{r}-\tau_j-\mathbf{R}_n) \rangle \end{aligned} \tag{2.48}$$

$$E_{\delta\mathrm{ee}} = \frac{1}{2}\int dr^3 \delta n(\mathbf{r}) \delta V_{\mathrm{H}}(\mathbf{r}) \tag{2.49}$$

$$E_{\mathrm{scc}} = \frac{1}{2}\sum_{I,J}\left\{ \frac{Z_I Z_J}{|\tau_I - \tau_J|} - \int dr^3 n^{(a)}_I(\mathbf{r}) V^{(a)}_{\mathrm{H},J}(\mathbf{r}-\tau_J) \right\} \tag{2.50}$$

Following the reorganization of energy terms, the total energy can be given by

$$E_{\mathrm{tot}} = E_{\mathrm{kin}} + E_{\mathrm{na}} + E^{(\mathrm{NL})}_{\mathrm{ec}} + E_{\delta\mathrm{ee}} + E_{\mathrm{xc}} + E_{\mathrm{scc}}. \tag{2.51}$$

2.6 Charge analysis

2.6.1 Mulliken population

As is the case with the previous section, the Kohn-Sham Bloch functions ψ_μ are expanded in a form of LCPAO $\phi_{i\alpha}$ centered on site τ_i by

$$\psi^{(\mathbf{k})}_{\sigma\mu}(\mathbf{r}) = \frac{1}{\sqrt{N}} \sum_n^N e^{i\mathbf{R}_n\cdot\mathbf{k}} \sum_{i\alpha} c^{(\mathbf{k})}_{\sigma\mu,i\alpha} \phi_{i\alpha}(\mathbf{r}-\tau_i-\mathbf{R}_n), \tag{2.52}$$

where *c* and ϕ are an expansion coefficient and pseudo-atomic function, $\mathbf{R}_n$ a lattice vector, *i* a site index, σ ($\uparrow$ and $\downarrow$) spin index, $\alpha \equiv (plm)$ an organized orbital index with a multiplicity index *p*, an angular momentum quantum number *l*, and a magnetic quantum number *m*. The charge density operator $\hat{n}_\sigma$ for the spin index σ is given by

$$\hat{n}_\sigma = \frac{1}{V_{\mathrm{B}}} \int_{\mathrm{B}} dk^3 \sum_\mu^{\mathrm{occ}} \left| \psi^{(\mathbf{k})}_{\sigma\mu} \right\rangle \left\langle \psi^{(\mathbf{k})}_{\sigma\mu} \right|, \tag{2.53}$$

where $\int_{\mathrm{B}}$ means the integration over the first Brillouin zone of which volume is V_{B}, and $\sum^{\mathrm{occ}}$ means the summation over occupied states. The charge density $n_\sigma(\mathbf{r})$ with the spin index σ is found as

$$n_\sigma(\mathbf{r}) = \sum_n^N \sum_{i\alpha,j\beta} \rho^{(\mathbf{R}_n)}_{\sigma,i\alpha,j\beta} \phi_{j\beta}(\mathbf{r}-\tau_j)\phi^*_{i\alpha}(\mathbf{r}-\tau_i-\mathbf{R}_n) \tag{2.54}$$

with a density matrix defined by

$$\rho^{(\mathbf{R}_n)}_{\sigma,i\alpha,j\beta} = \frac{1}{V_{\mathrm{B}}} \int_{\mathrm{B}} dk^3 \sum_\mu^{\mathrm{occ}} e^{i\mathbf{R}_n\cdot\mathbf{k}} c^{(\mathbf{k})*}_{\sigma\mu,i\alpha} c^{(\mathbf{k})}_{\sigma\mu,j\beta}. \tag{2.55}$$

Then, Mulliken populations $M_{\sigma,i\alpha}$ are given by

$$M_{\sigma,i\alpha} = \sum_n^N \sum_{j\beta} \rho^{(\mathbf{R}_n)}_{\sigma,i\alpha,j\beta} S^{(\mathbf{R}_n)}_{i\alpha,j\beta} \tag{2.56}$$

where $S^{(\mathbf{R}_n)}_{i\alpha,j\beta}$ is an overlap integral. Since the Mulliken population can be obtained by integrating equation (2.54) over real space, and by decomposing it into each contribution specified with σ and $i\alpha$, it can be confirmed that the sum of $M_{\sigma,i\alpha}$ gives the number of electron N_{ele} per unit cell as follows:

$$N_{\mathrm{ele}} = \sum_\sigma \sum_{i\alpha} M_{\sigma,i\alpha}. \tag{2.57}$$

2.6.2 Voronoi Charge

The fuzzy cell method decomposes real space into smeared Voronoi cells, called the fuzzy cell[44]. The fuzzy cell at the site *i* is determined by a weighting function $\omega_i(\mathbf{r})$:

$$\omega_i(\mathbf{r}) = \frac{p_i(\mathbf{r})}{\sum_j p_j(\mathbf{r})} \tag{2.58}$$

with p_i defined by

$$p_i(\mathbf{r}) = \prod_{j\neq i} s_k(\mu_{ij}) \tag{2.59}$$

$$\mu_{ij} = \frac{r_i - r_j}{\tau_{ij}} \tag{2.60}$$

$$r_i = |\mathbf{r}-\tau_i|, \quad r_j = |\mathbf{r}-\tau_j|, \quad \tau_{ij} = |\tau_i - \tau_j| \tag{2.61}$$

$$s_k(x) = \frac{1}{2}\left\{1 - f_k(x)\right\} \tag{2.62}$$

$$f_k(x) = f_0\left(f_{k-1}(x)\right), \quad f_0 = \frac{3}{2}x - \frac{1}{2}x^3 \tag{2.63}$$

where $k = 3$ is chosen in OpenMX. As *k* increases the fuzzy cells defined by ω approach to Voronoi cells (Wigner-Seitz cells). From the definition equation (2.58) it is clear that

$$\sum_i \omega_i(\mathbf{r}) = 1. \tag{2.64}$$

Thus, the integration of the charge density equation (2.54) over real space can be decomposed by employing the weighting functions as follows:

$$\begin{aligned} \int dr^3 n_\sigma(\mathbf{r}) &= \int dr^3 \left[\sum_i \omega_i(\mathbf{r})\right] n_\sigma(\mathbf{r}) \\ &= \sum_i \int dr^3 \omega_i(\mathbf{r}) n_\sigma(\mathbf{r}) \end{aligned} \tag{2.65}$$

Thus, the Voronoi charge $N_{\sigma,i}$ at the site *i* can be defined by

$$N_{\sigma,i} = \int dr^3 \omega_i(\mathbf{r}) n_\sigma(\mathbf{r}). \tag{2.66}$$

From equation (2.65), it is confirmed that

$$N_{\mathrm{ele}} = \sum_\sigma \sum_i N_{\sigma,i}. \tag{2.67}$$

Chapter 3

Zigzag graphene nanoribbons on Ni(111)

In this Chapter, I study the magnetism in the ZGNR on Ni(111) substrate. The freestanding ZGNR has the peculiar electronic and magnetic features depending on the localized edge state and has a great potential for future spintronics applications. Two edges have opposite spin directions and accordingly the ground state is the AFM state and not the FM state. However, FM or ferrimagnetic properties are required for spintronics applications. I previously reported that the magnetism of the ZGNR is controlled by carrier doping and achieve the finite magnetization[22]. On the other hand, carrier doping is spontaneously induced by the charge transfer from the substrate. Therefore, it is expected that the magnetic state of the ZGNR can be controlled by the charge transfer from the substrate.

I perform the first-principles calculation for the ZGNR on Ni(111) substrate and ZGNR over a graphene sheet on Ni(111) [ZGNR/graphene on Ni(111)] substrate and clarify the magnetism in those. Because the lattice constant of Fcc Ni(111) and graphene are nearly commensurate[34], I study the ZGNR on Ni(111) substrate. I find that magnetic moments at the edges are very small in the monolayer ZGNR on Ni(111) and are substantial in ZGNR/graphene on Ni(111). The FM spin ordering between both edge C atoms is achieved at the ZGNR layer in ZGNR/graphene on Ni(111). Electron doping is induced by the charge transfer from the Ni(111) to ZGNR and the orbital hybridization between the edge C atom at the ZGNR and Ni(111) occurs. These features are expected to have a significant effect on the energetics of the magnetic state in

ZGNR/graphene on Ni(111).

3.1 Monolayer zigzag graphene nanoribbon on Ni(111)

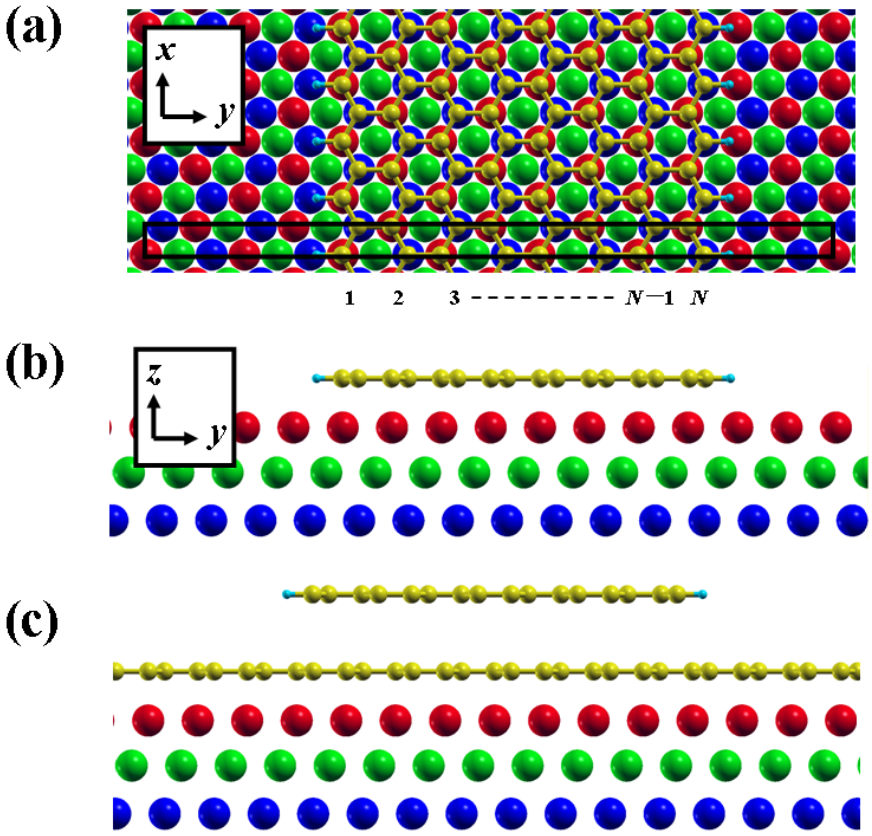

Figure 3.1: Atomic structure of the ZGNRs ($N = 8$) on Ni(111). The yellow and light blue spheres denote C and H atoms, respectively. The red, green and blue spheres denote the Ni atom at the first, second and third layers, respectively. (a) and (b) show the *xy*-plane and *yz*-plane for the monolayer ZGNR on Ni(111). The rectangle in (a) denotes the unit cell and *N* represents the ribbon width of the ZGNR. (c) shows the *yz*-plane for the ZGNR/graphene on Ni(111).

I first study the monolayer ZGNR on the Ni(111) substrate [Fig. 3.1 (a) and (b)]. By using the OPENMX code[43], I perform first-principles electronic-structure calculations based on the density functional theory (DFT) within the generalized gradient approximation (GGA)[40]. The norm-conserving pseudopotential method[45] is used. I use the linear combination of multiple

pseudo atomic orbitals generated by a confinement scheme[46, 47]. The orbitals are specified by H5.0-s2p1, C5.0-s2p2 and Ni6.0-s2p2d2: for an example, in the case of the C atom, C5.0-s2p2 means that the cutoff radius is 5.0 bohr in the generation by the confinement scheme[46, 47], and two primitive orbitals for each of *s* and *p* components are used. The partial core correction[48] is carried out for C and Ni atoms. The magnetic moment for each atom is estimated by a fuzzy cell partitioning method[44].

I use slab models to simulate the two systems in Fig. 3.1. The ribbon width N of the ZGNR is taken to be 8 [Fig. 3.1 (a)] and the unit cell includes 16 C, 2 H and 42 Ni atoms. I sample 30 k points in the periodic direction (x-direction): the total energy varies within only 0.04 meV/cell when 40 k points are used. The ZGNRs in the ribbon direction (y-direction) are separated by 12.1Å. The number of Ni(111) layers are taken to be three and the length of the vacuum region in the z-direction is 10.5Å. When the number of Ni layers is taken to be 4, the most stable spin configuration does not change. The lattice constant in the x-direction is taken to be 2.49Å which is $1/\sqrt{2}$ of the fcc Ni lattice constant 3.52Å. The value of the lattice constant 2.49Å corresponds to the fact that the lattice of the graphene expands by 1.2 %. This stretched lattice is found to have a negligible effect on the magnetic state: in the case of the freestanding ZGNR, the stretching varies the difference between the total energies of the APIES and PIES states by only 0.2 meV/cell. I use the interlayer distance determined by the low-energy electron diffraction experiment[34]: the distances between the ZGNR and first Ni layer, between the first and second Ni layers and between the second and third Ni layers are 2.14Å, 1.96Å and 2.09Å, respectively. The relative horizontal (x-y) positions of the C honeycomb structure to those of the Ni(111) surface are taken to be the same as those of the experiment[34].

In section 3.3, I will study the ZGNR/graphene on Ni. As was mentioned above, I use the experimental values for the positions of the C honeycomb structure of the graphene on the Ni(111) surface. When I optimize the relative horizontal (x-y) positions of the C honeycomb structure to those of the Ni(111) surface, the atomic position is relaxed within 0.05 Å and thus this relaxation effect on the energetics can be neglected. Actually I find that the relative energies among the three magnetic states studied in Sec. 3.3 vary by at most 0.4meV/cell.

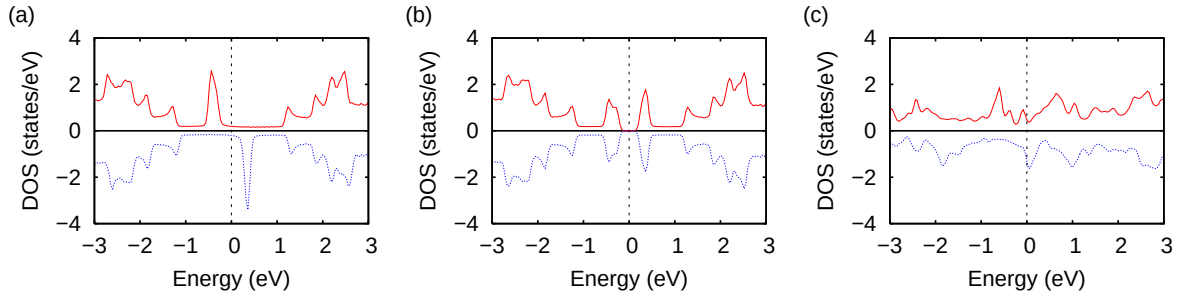

Figure 3.2: DOS of freestanding ZGNRs having the PIES (a) and APIES (b) state, respectively. The PDOS of the ZGNR on Ni(111) is shown in (c). The energy is measured from the Fermi energy. The solid and dashed lines denote the up and down spin states, respectively.

In the case of the ZGNR/graphene on Ni(111), I use the *AB*-stacking structure for the ZGNR and graphene sheet, and the interlayer distance between the ZGNR and graphene is 3.35 Å, which is taken to be the same as the experimental interlayer distance of graphite. In the cases of freestanding ZGNRs having the APIES and PIES states, the peaks of the density of states (DOS) originating from the edge state appear near the Fermi energies [Fig. 3.2 (a) and (b)][8, 18]. On the other hand, these peaks disappear in the case of the ZGNR on Ni(111) [Fig. 3.2 (c)] due to strong orbital hybridization between edge-localized p-orbitals and Ni d-orbitals. The magnetic moments of the ZGNR on Ni(111) are not localized at the edges and are broadly distributed (Fig. 3.3). The atomic magnetic moment averaged over the C atoms in the ZGNR is less than 0.05 $\mu_{\rm B}$/atom and is much smaller than those of freestanding ZGNRs having the APIES (0.25 $\mu_{\rm B}$/atom) and PIES (0.24 $\mu_{\rm B}$/atom) states at the edges. Therefore ZGNRs directly adsorbed on Ni(111) do not show *flat-band magnetism.* As is seen in Fig. 3.3, antiferromagnetic (AFM) coupling between the A and B sublattices is prominent. The projected density of states (PDOS) for all Ni atoms is similar to the DOS of the isolated Ni substrate (Fig. 3.4). The averaged atomic magnetic moment of the first Ni layer is 0.59 $\mu_{\rm B}$/atom which is somewhat smaller than that of the isolated Ni substrate (0.66 $\mu_{\rm B}$/atom).

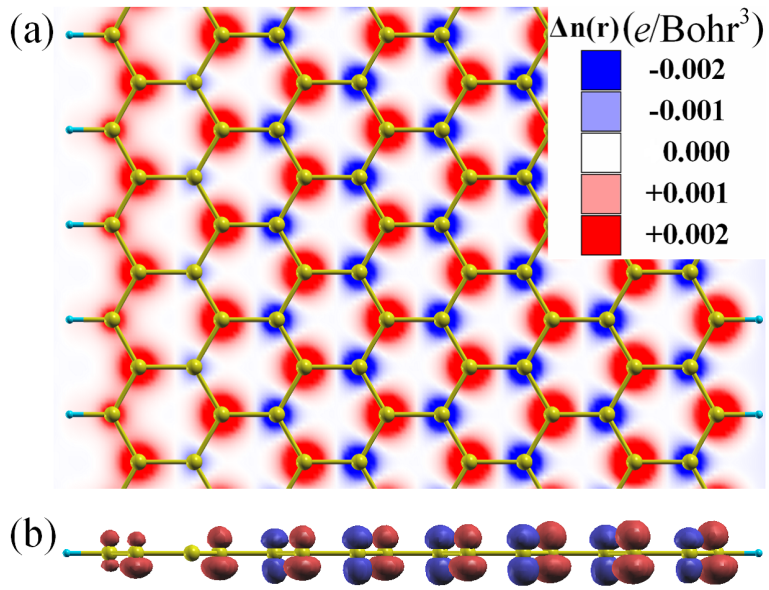

Figure 3.3: Spin densities of the monolayer ZGNR on Ni(111). (a) The spatial distribution of spin density on the *xy*-plane. The difference between the spin densities of the majority (up) and minority (down) components is presented. (b) The side view of the spin density. The red and blue denote the up and down spin states, respectively. The isovalues are 0.002 e/Bohr^3

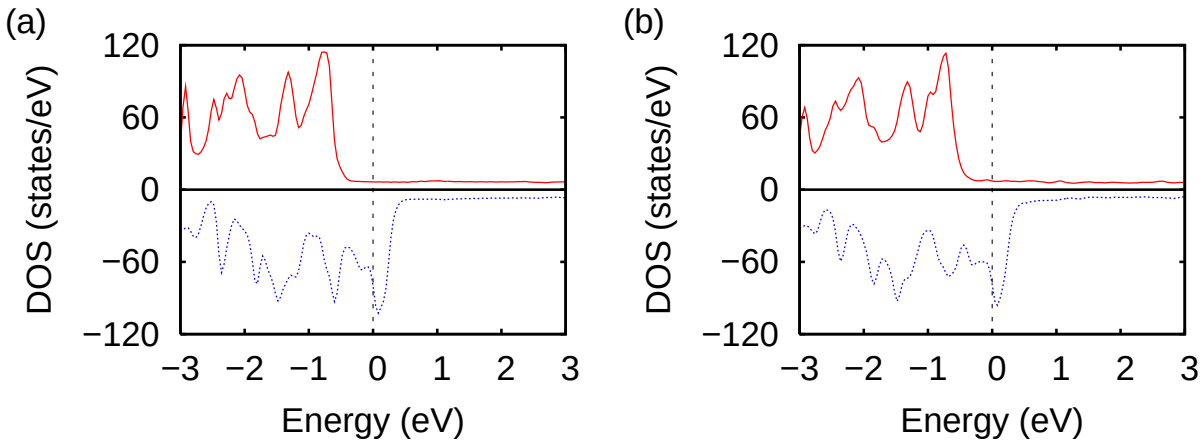

Figure 3.4: DOS of Ni atom. DOS of the isolated Ni substrate (a) and PDOS of the Ni substrate in the ZGNR on Ni(111) (b). The solid and dashed lines denote the up and down spin states, respectively. The energy is measured from the Fermi energy.

3.2 Graphene on Ni(111)

I next study the graphene on Ni(111). I use the unit cell which includes the 2 C and 3 Ni atoms. Whereas the isolated graphene has the NM ground state, the graphene on Ni(111) has magnetic moments. Therefore, the PDOS for the graphene is drastically modified due to the effect of the FM Ni substrate (Fig. 3.5): whereas the DOS is zero at the Fermi level in the freestanding graphene [Fig. 3.5 (a)], the DOS is not zero in the case of the graphene on Ni(111) [Fig. 3.5 (b)]. I find AFM-like coupling between the A and B sublattices of the graphene, which is similar to that of the ZGNR on Ni(111) (Fig. 3.3). Since these two sublattices are nonequivalent because of the substrate, the magnetic moments are different: 0.021 $\mu_{\rm B}$/atom and 0.027 $\mu_{\rm B}$/atom for the up (majority) and down (minority) spin states, respectively.

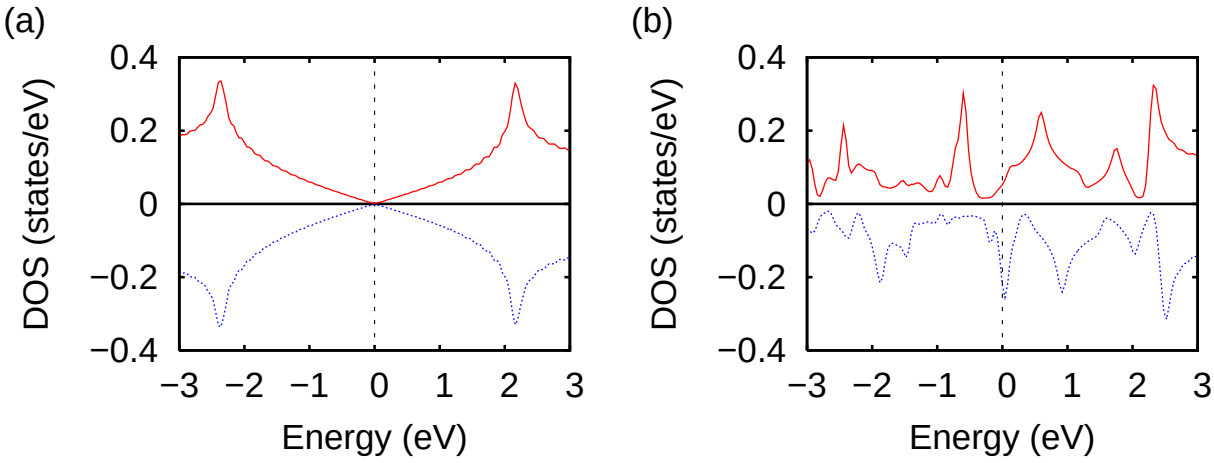

Figure 3.5: DOS of the isolated graphene (a) and PDOS of the graphene in the graphene on Ni(111) (b). Note that the isolated graphene is not AFM but NM. The solid and dashed lines denote the up and down spin states, respectively. The energy is measured from the Fermi energy.

3.3 ZGNR/Graphene on Ni(111)

Since it is expected that the graphene plays a role as a buffer layer on the Ni(111) substrate, I study the ZGNR/graphene on Ni(111) [Fig. 3.1 (c)]. I consider the APIES state as well as PIES-1 (PIES-2) state where the spin direction of the ZGNR is the same as (different from)

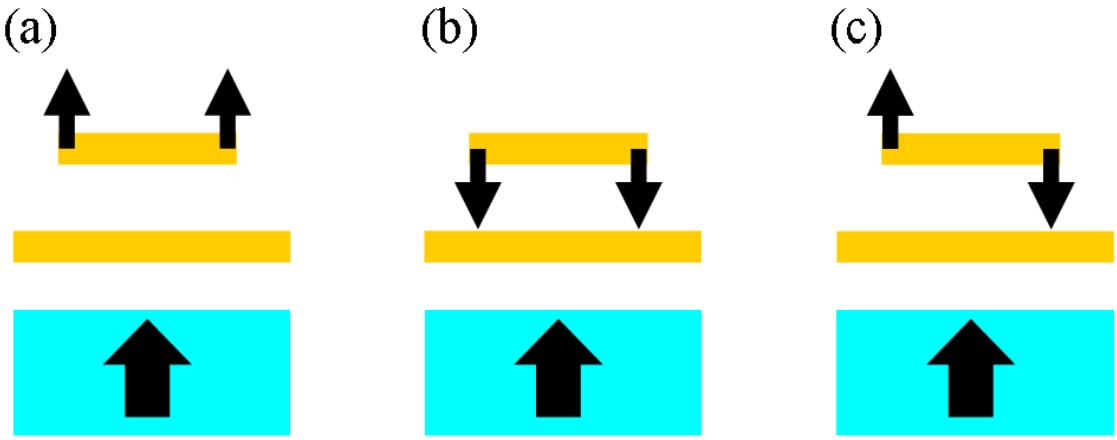

Figure 3.6: Magnetic structures of ZGNR/graphene on Ni(111). The PIES-1, PIES-2 and APIES states are shown in (a), (b) and (c), respectively. The short and long slabs denote the ZGNR and graphene sheet, respectively. The rectangle denotes the Ni layer. The black arrows denote the direction of magnetic moments.

that of the Ni substrate [Fig. 3.6]. I find that the PIES-1 state is the most stable: the difference between the total energies of the PIES-1 and APIES states is 4.2 meV/cell and that between the total energies of the PIES-1 and PIES-2 states is 5.9 meV/cell. In the cases that the ribbon widths are 9 and 10, the PIES-1 state is also found to be the most stable. These results show that the magnetic interaction between the ZGNR edges and Ni substrate is *ferromagnetic*. Whereas the localized edge state disappears in the ZGNR on Ni(111), the ZGNR/graphene on Ni(111) has the localized edge state (Fig. 3.7). The magnetic moments at the two edges of the PIES-1 state ZGNR are 0.18 $\mu_{\rm B}/{\rm atom}$ and 0.20 $\mu_{\rm B}/{\rm atom}$ which are close to that of the freestanding ZGNR having the PIES state (0.24 $\mu_{\rm B}/{\rm atom}$).

The PDOS of the graphene sheet in the ZGNR/graphene on Ni(111) are very similar among the three magnetic states [Fig. 3.8 (b), (d) and (f)] and are similar to the PDOS of the graphene sheet on Ni(111) [Fig. 3.5 (b)]. Therefore, the PDOS of the graphene is affected very little by top layer ZGNRs. The PDOS of the ZGNR having the PIES-1 state shows that the two peaks near the Fermi level are broadened whereas those of the freestanding ZGNR having the PIES state are sharp[Fig. 3.8 (a) and Fig. 3.2 (a)]. On the other hand, the PDOS of the PIES-2 state

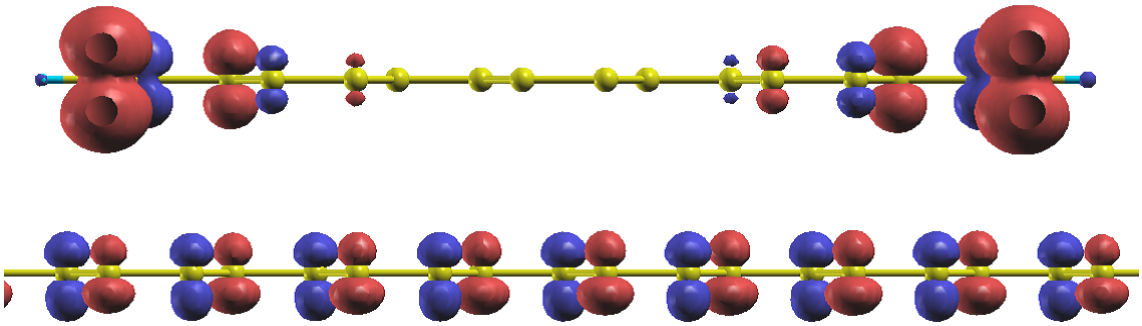

Figure 3.7: Isosurfaces of spin density of the PIES-1 state of ZGNR/graphene on Ni(111). The ZGNR plane (upper line) and graphene one(lower line) are presented and the Ni substrate is omit. The red and blue isosurfaces denote the up and down spin states, respectively. These isovalues are 0.002 e/Bohr^3

is similar to that of the freestanding ZGNR having the PIES state [Fig. 3.8 (c) and Fig. 3.2 (a)].

Here I discuss the relation of the PDOS of ZGNRs and the magnetic stability. In the case of the PIES-1 state, the locations of the peaks of the up (majority) and down (minority) near the Fermi level of the ZGNR are similar to those of the graphene: the up and down peaks are placed below and above the Fermi level, respectively [Fig. 3.8 (a) and (b)]. These similar locations of the up and down peaks are expected to enhance the hybridization between the orbitals of the ZGNR and graphene and induce broadening of the PDOS of the ZGNR. On the other hand, in the case of the PIES-2 state, the PDOS peaks of the up and down spin states of the ZGNR are located above and below the Fermi level. Thus, the locations are opposite to those of the graphene where the peaks of the up and down spin states are located below and above the Fermi level. These opposite locations reduce the orbital hybridization and cause the fact that the peaks are not so broadened. The strong orbital hybridization of the PIES-1 state is expected to cause the fact that the PIES-1 state has lower energy than the PIES-2 state.

The peaks of the APIES state are somewhat broadened compared with those of the free-standing ZGNR having the APIES state [Fig. 3.8 (e) and Fig. 3.2 (b)]. This broadening due to the orbital hybridization is expected to lower the total energy of the APIES state. Therefore, its energy is lower than that of the PIES-2 state, though it is higher than that of the PIES-1 state.

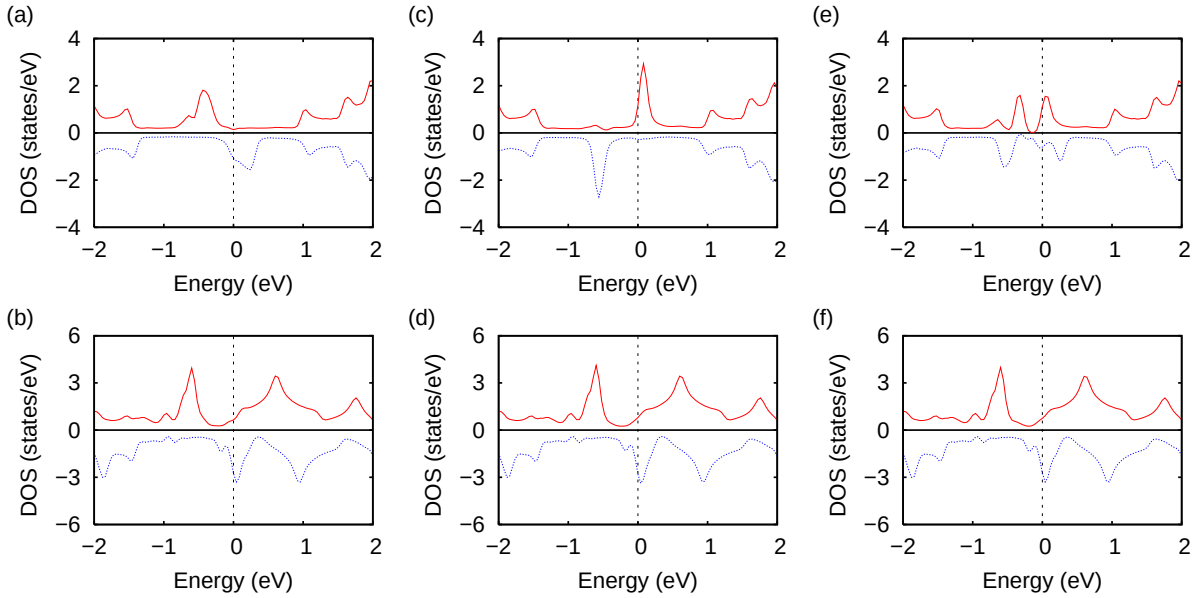

Figure 3.8: PDOS of the ZGNR and graphene sheet in ZGNR/graphene on Ni(111). The PDOS of the ZGNR for the PIES-1, PIES-2 and APIES states are shown in (a), (c) and (e), respectively and that of the graphene for the PIES-1, PIES-2 and APIES states are shown in (b), (d) and (f), respectively. The solid and dashed lines denote the up and down spin states, respectively. The energy is measured from the Fermi energy.

I have discussed the effect of the orbital hybridization. Beside the orbital hybridization effect, the charge transfer from the substrate into the ZGNR affects the magnetic stability as was shown in a previous study[22]. I find that electrons are injected into the ZGNR in the case of the three magnetic states. The Fermi level shifts upward from the case of the freestanding ZGNRs [Fig. 3.8 (a), (c), (e) and Fig. 3.2 (a), (b)]. For all three magnetic states, by using a fuzzy cell partitioning method[44], the number of injected electrons are estimated to be 0.1 *e*/cell in the ZGNR and 1.5 *e*/cell in the graphene sheet. The electron transfer from the substrate into the ZGNRs is expected to affect the magnetic stability. It is noted that previous DFT study of the graphene on Ni(111)[49] found the electron transfers from the Ni substrate to the graphene, which is consistent with our results.

3.4 Conclusion

I have performed first-principles DFT calculations to clarify the magnetism of the monolayer ZGNR on Ni(111) and ZGNR/graphene on Ni(111). I studied ZGNRs whose ribbon widths are 1.8 nm $\sim$ 2.2 nm. I found that the magnetic moments at the edges are small in the monolayer ZGNR on Ni(111) and do not show *flat-band magnetism*. On the other hand, in ZGNR/graphene on Ni(111), I found that magnetic moments of the edges are substantial and are close to those of the freestanding ZGNRs. The *flat-band magnetism* is recovered by the buffer graphene sheet. The magnetic ground state is the PIES-1 type [Fig. 3.6 (a)]. I reveal the orbital hybridization between the edge C atoms of the ZGNR and graphene and electron injection induced by the charge transfer from the Ni(111) substrate to ZGNR. These features are expected to have a significant effect on the energetics of the magnetic state.

It is well known that the APIES state is the ground state of the freestanding ZGNR. However, I found that the PIES-1 state has 4.2 meV/cell lower energy than the APIES state in the ZGNR/graphene on Ni(111). In the ZGNR on the Ni substrate, the monolayer ZGNR on the Ni substrate dose not have the magnetic moment at edge C atoms and becomes buffer layer. In the ZGNR over a graphene sheet on the Ni substrate, the magnetic moment maintains at edge C atoms and becomes FM state by the orbital hybridization and electron doping. If the magnetic nano device is constructed, it is necessary that the ZGNR is allocated at the second layer. Therefore, this study demonstrated that substrates have significant effects on the magnetism of ZGNRs. This finding is important for device applications of ZGNRs.

Chapter 4

Dehydrogenated armchair graphene nanoribbon

In this Chapter, I study the magnetism in the dehydrogenated AGNR. AGNRs are energetically more stable than the ZGNR[36] and thus offten observed than the zigzag edge in the edge of graphene experimentally[37]. Although AGMRs are stable, they have nonmagnetic property, apllication of this ribbon to spintronics has not been studied. Compared with hydrogenated GNRs, the magnetic property of dehydrogenated GNRs is insufficient, although there are some theoretical works on the stability of dehydrogenated AGNRs[36, 37, 50, 51].

I perform the first-principles calculation for the dehydrogenated AGNR. Although the zigzag graphene nanoribbon attracts scientific interest because of its magnetic properties, the study of the magnetism of AGNRs is insufficient. I find that the magnetic state of dehydrogenated AGNRs is stable in a wide range of electron doping. The spin polarization originates from the localized edge state around the Brillouin zone boundary. In the case of field effect transistor doping, some of the electrons injected into indirect-gap AGNRs induce half-metallicity and heavily doped direct-gap AGNRs are antiferromagnetic. I also find that nitrogen doping produces ferromagnetic insulators and half-metals.

4.1 Nondoped dehydrogenated AGNR

I study the dehydrogenated AGNR. I perform first-principles electronic-structure calculations based on the density functional theory. The exchange correlation potential is based on the spin-polarized generalized gradient approximation[40] and norm-conserving pseudopotentials[45] with a partial core correction[48] are used. Wavefunctions are expanded by a linear combination of multiple pseudo atomic orbitals[46, 47]: two *s*-orbitals and two *p*-orbitals of the C atom are used. I confirm that the convergence of the total energy for the basis set is within 0.6 meV/cell. 60 *k* points are used in the Brillouin zone integration; the total energy varies within 0.01 meV/cell when 120 *k* points are used. I perform geometry optimization for each spin configuration. All the calculations are performed by using the OPENMX code[43].

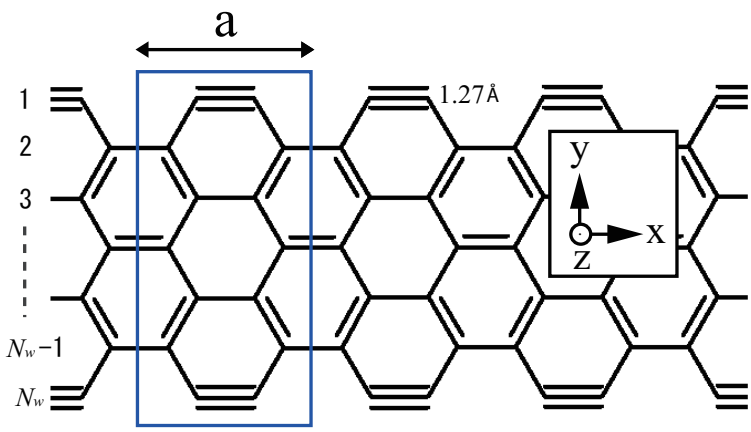

Figure 4.1: Lattice structures of AGNR. The rectangle with solid lines is the unit cell and a is the lattice constant. N_w is the width of the AGNR.

First, I study the geometry of the nondoped dehydrogenated AGNR in the case of N_w = 7, where N_w denotes the ribbon width (Fig. 4.1). I start self-consistent calculations by determining the initial magnetic configurations of the PIES [Fig. 4.2 (a)] and APIES [Fig. 4.2 (b)] states, and find that the final magnetic state is NM. These results indicate that the PIES and APIES states are unstable and only the NM state is stable. The bond length between the edge C atoms is 1.27 Å, which is smaller than that of pristine graphene (1.42 Å). This short bond corresponds

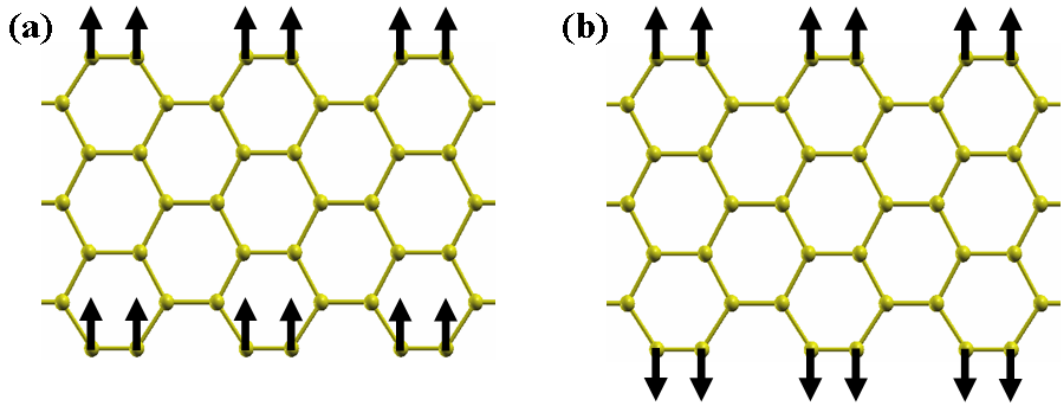

Figure 4.2: Magnetic structures of the dehydrogenated AGNR. (a) and (b) show the PIES and APIES states, respectively. The arrows represent relative spin directions between different sites. (The absolute spin directions are not determined in the present calculation since I neglect the spin-orbit interaction.)

to a triple bond and induces a large indirect band gap [Fig. 4.3 (a)]. As a result, this AGNR is an NM insulator. The valence band top is located at the Γ-point, whereas the conduction band bottom is located at the X-point (X = π/a).

The wavefunctions of the lowest and second-lowest unoccupied states at the X-point are shown in Figs. 4.3 (b) and 4.3 (c), respectively. The signs at the two edges are the same [different] in Fig. 4.3 (b) [Fig. 4.3 (c)]. As a result, the former wavefunction has a 0.17 eV lower energy than the latter wavefunction. The dispersions of the two bands located near the X-point are small; thus, electron doping is expected to induce magnetism.

Since triple bonds are formed at the edges, the electronic structure of the dehydrogenated AGNR is different from that of the hydrogenated AGNR. The lowest conduction band consists of σ orbitals, whereas the magnetism of the doped hydrogenated AGNR originates from π orbitals[38].

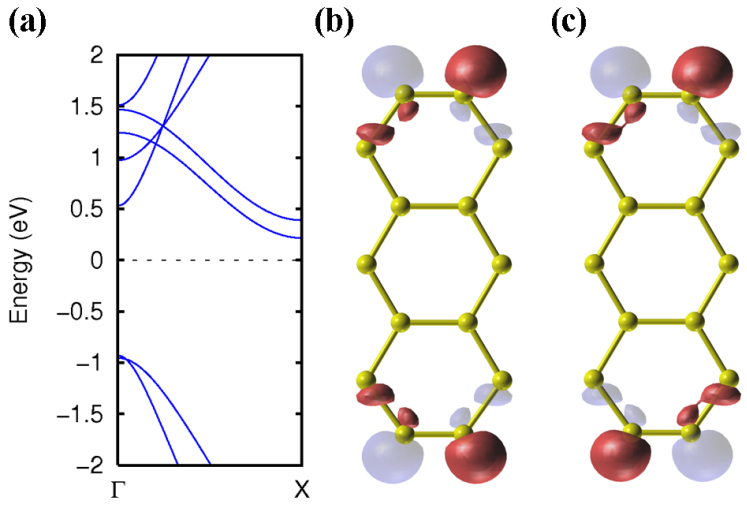

Figure 4.3: Electronic structures of the dehydrogenated AGNR. (a) shows the band structure of the NM state. The Fermi level is set to be zero. (b) and (c) show the lowest and second-lowest unoccupied molecular orbitals at the X-point, respectively. The red (dark) and blue (bright) isosurfaces indicate the positive and negative amplitudes of the wavefunctions, respectively. The absolute isovalues are 0.075/Bohr$^{3/2}$.

4.2 Electron-doped dehydrogenated AGNR

Here, I study the electron-doped AGNR by using the Fermi level shift (FLS) method: When the electron is injected into the unit cell, I introduce a uniform positive background charge to make the system neutral. I first investigate the magnetic state of the AGNR when the electron concentration x is 0.2 e/cell. Geometry optimization is performed and the bond length of the edge C atoms is found to be 1.28 Å. This bond length is slightly larger than that in the nondoped case (1.27 Å) owing to the fact that electrons occupy the lowest antibonding character band [Fig. 4.3 (b)]. In the PIES state, the parallel configuration of the two FM chains located at both edges [Fig. 4.2 (a)] is more stable than that in the NM state. The difference between the total energies of the PIES and NM states is 2.4 meV/cell. As shown by the band structure and density of states in Fig. 4.4, the most stable PIES state has a *half-metallic* property. This spin polarization originates from the localized edge state around the X-point, as shown in Fig. 4.3 (b) or 4.3 (c). Such edge-localized spin polarization reminds us of the flat-band ferromagnetism originating from the localized edge state in the ZGNR.

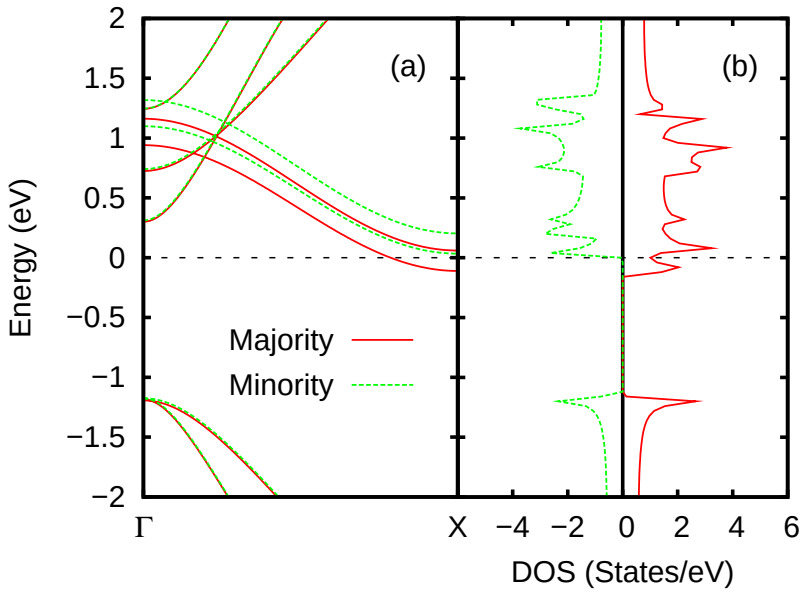

Figure 4.4: Band structure (a) and density of states (b) of the PIES state when x = 0.2 e/cell. The solid and dashed lines denote the majority and minority spin states, respectively. The Fermi level is set to be zero.

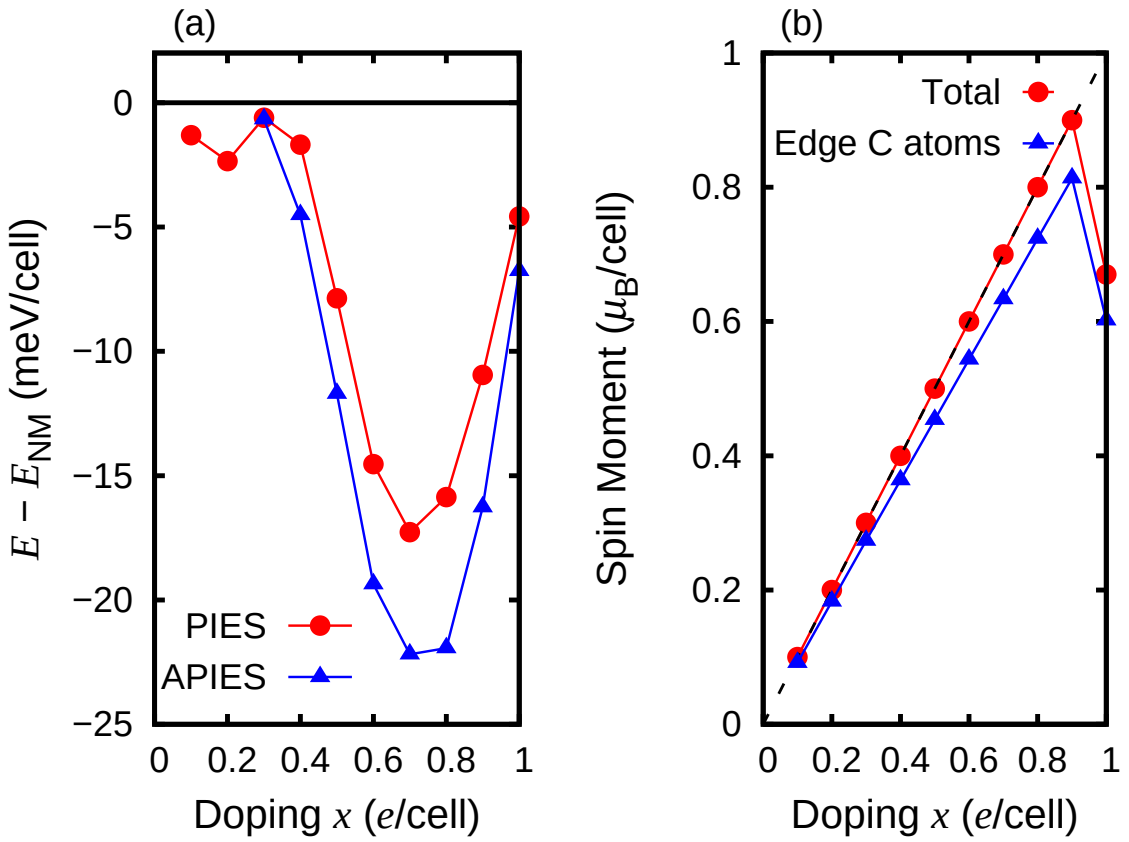

Figure 4.5: (a) Total energy measured from that of the NM state as a function of x. Circles and triangles denote the PIES and APIES states, respectively. (b) Total spin moment (circles) and the sum of spin moments of edge C atoms (triangles) for the PIES state as a function of x.

I examine various AFM states and find that they are unstable. The APIES state shown in Fig. 4.2 (b) and the AFM chains at the edges are unstable. By using a double-size cell, I calculate the chain of the AFM configuration of the FM dimers and find that this state is also unstable. I study the electron carrier concentration dependence of magnetic states in the AGNR. Figure 4.5 (a) shows the relative total energies of the PIES, APIES, and NM states. When x = 0.1 and 0.2 e/cell, the PIES state is the ground state and the NM and APIES states are metastable and unstable, respectively. In the region where $0.3\ e/\mathrm{cell} \leq x \leq 1.0\ e/\mathrm{cell}$, the APIES state has the lowest energy and the NM and PIES states are metastable. Figure 4.5 (b) shows that the total spin moment of the PIES state mainly originates from the edge C atoms.

In Fig. 4.6, I show the band structures of the metastable PIES state when x = 0.4 and 0.7

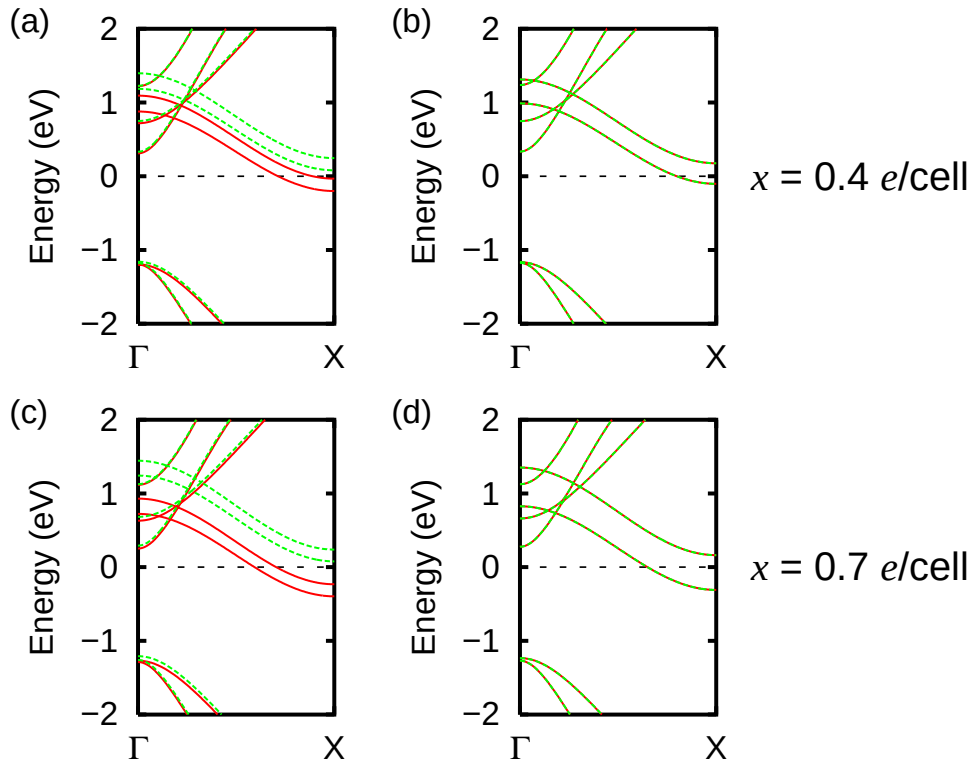

Figure 4.6: Band structures of the (a) PIES and (b) APIES states when $x = 0.4$ *e*/cell, and the (c) PIES and (d) APIES states when $x = 0.7$ *e*/cell. The solid and dashed lines in (a) and (c) denote the majority and minority spin states, respectively. The Fermi level is set to be zero.

e/cell. The difference between the energies of the majority and minority spin conduction bands at the X-point increases when x increases from 0.2 *e*/cell (Fig. 4.4) to 0.7 *e*/cell (Fig. 4.6). Therefore, even when x is large ($0.3\ e/\text{cell} \leq x \leq 0.9\ e/\text{cell}$), all the injected electrons still occupy the two majority spin bands. As a result, the system shows a half-metallic property when $0.1\ e/\text{cell} \leq x \leq 0.9\ e/\text{cell}$. However, when $x = 1.0$ *e*/cell, the minority spin band is partially occupied; thus, the system is not half-metal. As shown in Fig. 4.5 (b), the total spin moment is proportional to x when $0.1\ e/\text{cell} \leq x \leq 0.9\ e/\text{cell}$, which indicates that this system is a half-metal.

In the APIES state, the two spin bands are degenerated (Fig. 4.6). In the case of $0.3\ e/\text{cell} \leq x \leq 1.0\ e/\text{cell}$, the injected electrons partially occupy the lowest conduction band whose wavefunctions have the same phase at the two edges. This is in contrast to the PIES state: The injected electrons occupy the two majority-spin bands whose wavefunctions have the same and

opposite phases when $0.3\ e/\mathrm{cell} \leq x \leq 1.0\ e/\mathrm{cell}$. This occupation of the second-lowest conduction band is expected to increase the total energy of the PIES state.

As mentioned above, when $x \geq 0.3\ e/\mathrm{cell}$, the APIES state is the ground state and the PIES state has a higher energy than the APIES one. Even in this case, the ground PIES state is expected to be achieved by the following two ways. If magnetic fields whose directions are the same at both edges are introduced, the PIES state becomes the ground state, as was discussed in a previous study[52]. The magnetic field converting the energetical order ranges from 67 to 73 T, which is estimated from the total energy difference between the PIES and APIES states (x = 0.4 - 0.8 *e*/cell). I propose another method. Ferromagnets, such as Fe, Co, and Ni, are used to flip the edge spin in electron-doped AGNRs: Ferromagnets are located on both sides of AGNRs. If the exchange interaction between the edge atoms and the ferromagnet is larger than that between carbon atoms at both edges, the magnetic state of AGNRs can be controlled by the spin direction of ferromagnets: the PIES state can be achieved when ferromagnets on both sides have the same spin direction.

Here, I examine the stability of the PIES state in highly doped AGNRs. When x = 0.1 *e*/cell and 0.2 *e*/cell, the PIES state is the ground state and the difference between the energies of the PIES and NM states is small (1.3 and 2.4 meV/cell, respectively). On the other hand, when x = 0.7 *e*/cell, the difference between the total energies of the PIES and NM states increase (17.3 meV/cell), though the APIES state is the ground state. Therefore, if I can achieve the situation where the PIES state has a much lower energy than the APIES state by using the methods mentioned above, the system is expected to be thermally stable.

As mentioned above, I found that half-metallicity can be achieved when an electron is injected into the lowest conduction band at the X-point. Here, I discuss the relationship between the ribbon width (N_w) and the energetical order of the Γ- and X-points. As shown in Fig. 4.7, the energy of the lowest conduction band at the X-point measured from that at the Γ-point tends to increase with N_w. The difference between the energies at the Γ- and X-points when $N_w = 3n + 1$ tends to be higher than those when $N_w = 3n$ and $3n + 2$. This three-time cycle is expected to originate from the quantum confinement, as was discussed in the case of hydro-

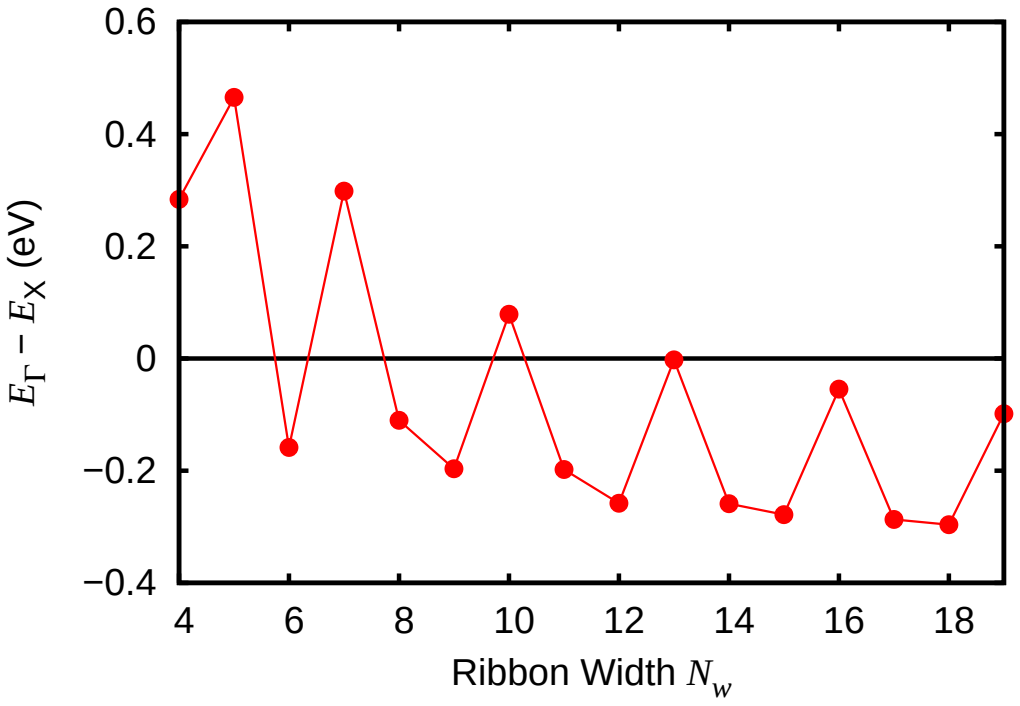

Figure 4.7: Difference between the lowest conduction-band energies at the Γ and X points as a function of N_w.

genated AGNRs[53]. I find that the conduction-band bottom is located at the X-point when N_w = 4, 5, 7, and 10. In the case of N_w = 7, the system is made half-metallic by a certain amount of electron doping, as was mentioned (Fig. 4.5). In the cases of N_w = 4, 5, and 10, I also find that half-metallicity is achieved by doping.

When the energy level of the Γ-point of the lowest conduction band is lower than that of the X-point, the levels near the X-point are not occupied in the case of lightly electron doped AGNR; therefore, the system is found to be NM. However, heavy electron doping leads to the occupation of the lowest conduction band near the X-point and leads to a magnetic state: I examine the direct-gap AGNRs whose N_w is up to 16 and confirm that heavy electron doping induces the APIES ground state.

4.3 Nitrogen-doped dehydrogenated AGNR

Thus far, I studied the electron-doped AGNR by using the FLS method. The doping is expected to be possible by using the field effect transistor (FET) method. Here, I demonstrate that chemical doping can also be performed, as was discussed in a previous study on the ZGNR[22]. It was reported that substitutional boron impurities induce p-type carbon nanotubes[54, 55] and n-type graphene is formed by nitrogen impurities[56]. I here study the N-substituted impurities. In the AGNR (N_w = 7), nitrogen atoms are located at the central part in the super cell that includes 140 host atom sites [Figs. 4.8 (a), 4.8 (c), and 4.8 (e)]. I optimize the geometry and find that the substituted atoms are located on the graphene plane. I find that the PIES state is the ground state, the NM sate is metastable, and *the APIES state is unstable*. The difference between the total energies of the NM and PIES states is shown in Table I. When *x* is small (0.1 - 0.3 *e*/cell), the system is an FM insulator. As shown in Figs. 4.8 (a), 4.8 (c), and 4.8 (e), the spin density is localized in the edge region, which is near the nitrogen atoms. This is due to the fact that electrons feel the attractive potential from the nitrogen atom. This localization reduces the band dispersion, and then, the systems are insulators [Figs. 4.8 (b) and 4.8 (d)]. As *x* increases, the spin densities become delocalized; thus, the band dispersions are large [Fig. 4.8 (f)]. As a result, when *x* = 0.4 and 0.5 *e*/cell, the systems are half-metals.

As shown in Table 4.1, the difference between the total energies of the PIES and NM states in the case of chemical doping is larger than that in the case of FET doping. Moreover, since there are no minority spin bands around the Fermi level in the nitrogen-doped half-metallic AGNR as shown in Fig. 4.8 (f), the half-metallic property is thermally robust. Therefore, it is considered that chemical doping is more favorable than FET doping.

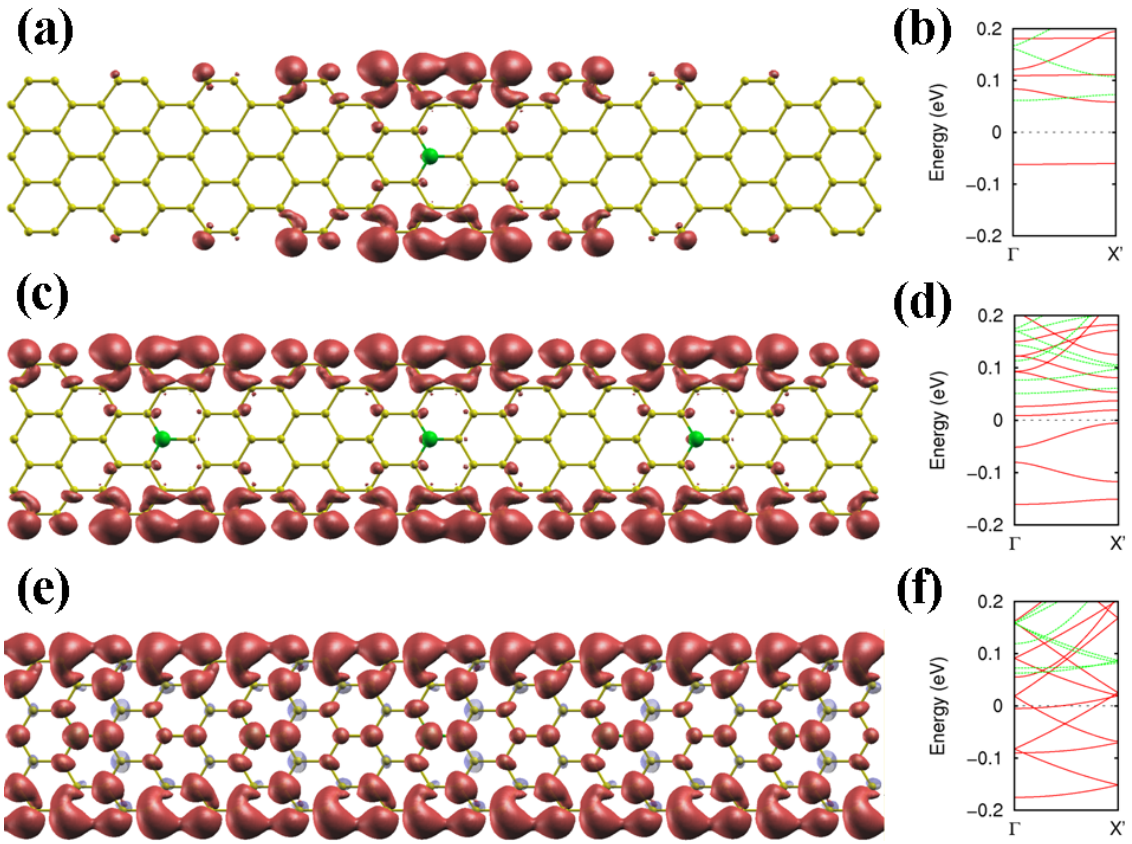

Figure 4.8: Difference between the lowest conduction-band energies at the Γ and X points as a function of N_w.

Table 4.1: Total energy difference between the NM and PIES states [ΔE = E_{PIES} - E_{NM} (meV/cell)] as a function of electron carrier concentrations x. The calculated results in the cases of the chemical doping (Chem) and Fermi-level shift (FLS) are tabulated. I and M denote the FM insulator and half-metal, respectively.

	ΔE (meV/cell)	
x (e/cell)	Chem	FLS
0.1	-4.9 (I)	-1.3 (M)
0.2	-7.8 (I)	-2.4 (M)
0.3	-5.0 (I)	-0.6 (M)
0.4	-6.6 (M)	-1.7 (M)
0.5	-5.9 (M)	-7.9 (M)

4.4 Conclusion

I have performed density-functional calculations on dehydrogenated AGNRs. Although dehydrogenated AGNRs are considered to be irrelevant to magnetism, I find that the magnetic state of AGNRs is stable in a wide range of electron doping. The spin polarization originates from the localized edge state around the Brillouin zone boundary.

I studied doped AGNRs by using the FLS method calculations, which are expected to correspond to those in the case of FET doping. When N_w = 7, the PIES state is the ground state when x = 0.1 and 0.2 *e*/cell. This PIES state is found to have half-metallic characters. The APIES state is the ground state when $0.3\ e/\mathrm{cell} \leq x \leq 1.0\ e/\mathrm{cell}$. The metastable PIES state when $0.3\ e/\mathrm{cell} \leq x \leq 1.0\ e/\mathrm{cell}$ is expected to be the most stable when the magnetic field is introduced or the ferromagnets at both edges are introduced. I found that electron-doped AGNRs are half-metals when N_w = 4, 5, 7, and 10, and the APIES state of AGNRs, whose N_w is up to 16, is induced by heavy electron doping.

I also studied N doping. When N_w = 7, the PIES state is the most stable and the APIES state is unstable. When $0.1\ e/\mathrm{cell} \leq x \leq 0.3\ e/\mathrm{cell}$, the system is an *FM insulator* and is expected to be useful for spintronics applications. When x = 0.4 and 0.5 *e*/cell, the system is a half-metal, which is more stable than that in the case of FET doping.

The armchair edges of graphenes are often experimentally observed compared with the zigzag edges of graphenes owing to the fact that the former edges are energetically favorable[36, 37]. The dehydrogenation of AGNRs can be achieved by elevating temperature, and dehydrogenated AGNRs are very stable since triple bonds are formed at the edges[36, 37, 50, 51, 57]. Therefore, electron-doped dehydrogenated AGNRs are expected to be suitable for nanospintronics applications.

Chapter 5

Summary

5.1 Conclusion

Since the magnetism of the ZGNR was theoretically proposed[8], a lot of works have been carried out. In this work, I studied the effect of the Ni(111) substrate on the magnetism of the ZGNR and the effect of the carrier doping on the magnetism of the dehydrogenated AGNR. I have performed the first-principles calsulation for the monolayer ZGNR on Ni(111) and ZGNR/graphene on Ni(111) and crarified the the magnetism of the monolayer ZGNR on Ni(111) and ZGNR/graphene on Ni(111). I found that the magnetic moment of the edge C atom at the mono ZGNR on Ni(111) layer is very small due to the hybridization between π electron of the ZGNR and d electron of the first Ni layer. The electronic structure of the graphene was drastically modified due to the effect of the FM Ni substrate whereas that was zero at the Fermi level in the freestanding graphene. I found the slight spin polarization and AFM-like coupling between the A and B sublattices of the graphene. On the other hand, in the case of the ZGNR/graphene on Ni(111), the magnetic moment of the edge C atom at the ZGNR layer maintains and the FM state is the ground state. I indicated the orbital hybridization between the edge C atoms of the ZGNR and graphene and electron injection induced by the charge transfer from the Ni(111) substrate to ZGNR. These features are expected to have a significant effect on the energetics of the magnetic state. So the bilayer structure between the ZGNR and graphene

sheet is favorable from the viewpoint of spintronics application.

Next, I have performed the first-principles calculation on the dehydrogenated AGNR. Surprisingly, I found that dehydrogenated AGNR has a magnetic state in the case of carrier doping. Magnetic state of the carrier-induced AGNR has FM chains at the two edges having the same directions of the magnetic moments. I found that electron-doped AGNRs are half-metals in short ribbon width of AGNRs. I also studied N doping and found that the PIES state is the most stable. The system was an FM insulator and was expected to be useful for spintronics applications in the region of the low dpoing concentration. In the high doping concentration, the system is a half-metal, which is more stable than that in the case of FET doping. Therefore, electron-doped dehydrogenated AGNRs are expected to be suitable for nanospintronics applications.

I theoretically demonstrated that the GNR has the great potential for the spintronics application. Despite the magnetism in the graphene attract much attention, the magnetism with respect to carrier doping is hardly researched. In this regard, I previously realized the magnetic phase control of graphene-based materials by carrier doping and potentialized as the magnetic nano device[22]. In this work, I achieved that the magnetism in the ZGNR is also controlled by the effect of the substrate, orbital hybridization and charge transfer. On the other hand, the NM AGNR is magnetized by electron doping and became half-metal. Therefore, carrier-induced GNRs are very interest in terms of the nano spintronics device such as the magnetic sensor. Finally, I suggest that these findings open new possibility of carbon materials in the spintronics application.

5.2 Future plan

In order to investigate the property for spintronics devices, I examine the transport property in the GNR by means of the equilibrium Green's function (EGF) method. The EGF method is described in Appendix A. Previously, it is theoretically reported that spin-polarized transport properties are predicted[15, 58, 59]. However, these spin transport calculation is within the collinear magnetism. To closely investigate the spin transport property, I have to consider

the noncollinear magnetism and include the spin orbit interaction (SOI). Experimentally, the noncollinear magnetic structure at the surface and surface nanostructure can be observed directly by using the spin polarized scanning tunneling microscope[60]. In these surface and interface nanomagnetic structure, the anomalous and new phenomena related to the spin current is shown. Therefore, it is very interesting to calculate the transmission and current in the noncollinear spin structure. So, I am developing the transport calculation code included the noncollinear magnetism and SOI. Details of the method is presented in Appendix A. On the other hand, since the electronic structure of graphene drastically change by the effect of magnetic substrate, I have to perform the transport calculation for the system included the magnetic substrate. In future, I will perform the first-principles noncollinear transport calculation of the more realistic system such as the FET structure used GNRs (Fig. 5.1).

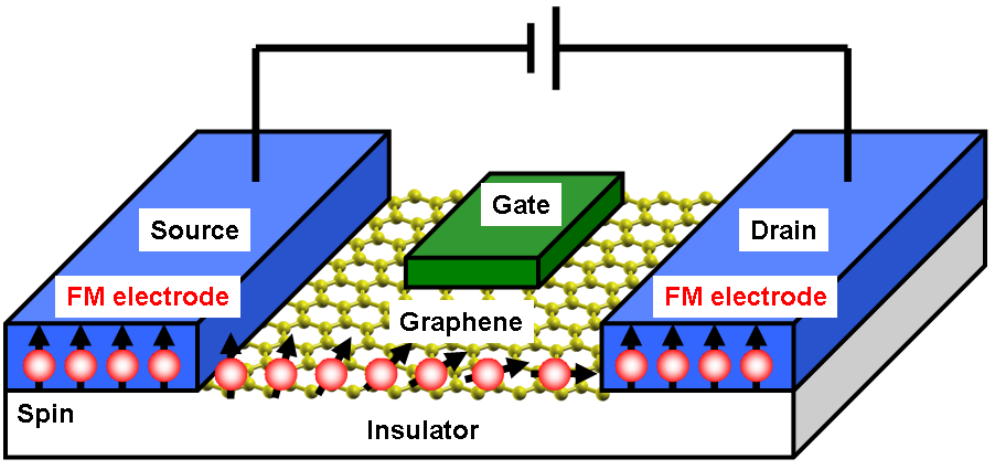

Figure 5.1: FET structure used graphene.

Appendix A

Equilibrium Green's function method

Equilibrium Green's function (EGF) methods are regularly used to calculate transmission and conductance in nanoscale conductors under non-vias. This method is mainly used for ballistic conduction but may be extended to include inelastic scattering. In this appendix, I explain the transport calculation of the EGF method by consulting references[61, 62].

A.1 Green's function

The system consists of a central region connected with infinite left and right leads as shown in Fig A.1.

To provide the simple explanations, I consider the one particle Green's function. Schrödinger equation:

$$H|n\rangle = E|n\rangle \tag{A.1}$$

I divide the Hamiltonian and wavefunction of the system into lead $(H_{\mathrm{L,R}}, |\psi_{\mathrm{L,R}}\rangle)$ and central region $(H_{\mathrm{C}}, |\psi_{\mathrm{C}}\rangle)$ subspaces:

$$\begin{pmatrix} H_{\sigma,\mathrm{L}} & \tau_{\sigma,\mathrm{L}} & 0 \\ \tau^{\dagger}_{\sigma,\mathrm{L}} & H_{\sigma,\mathrm{C}} & \tau^{\dagger}_{\sigma,\mathrm{R}} \\ 0 & \tau_{\sigma,\mathrm{R}} & H_{\sigma,\mathrm{R}} \end{pmatrix} \begin{pmatrix} |\psi_{\sigma,\mathrm{L}}\rangle \\ |\psi_{\sigma,\mathrm{C}}\rangle \\ |\psi_{\sigma,\mathrm{R}}\rangle \end{pmatrix} = E \begin{pmatrix} |\psi_{\sigma,\mathrm{L}}\rangle \\ |\psi_{\sigma,\mathrm{C}}\rangle \\ |\psi_{\sigma,\mathrm{R}}\rangle \end{pmatrix} \tag{A.2}$$

where σ is the index for the spin, $\tau_{\sigma,\mathrm{L,R}}$ describes the interaction between leads and central

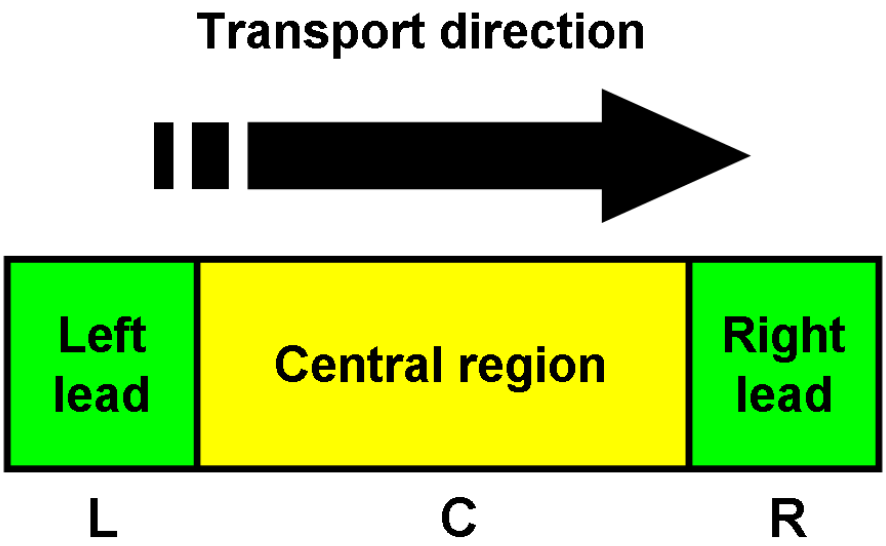

Figure A.1: Configuration of the system treated by EGF method

region. Here, I will assume that the leads are independent, i.e., there are no cross terms (τ) between the different leads. The Green's function is defined as

$$(E - H)G(E) = I. \tag{A.3}$$

The Green's function gives the response of a system to a constant perturbation in the Schrödinger equation. For example, from third row of equation (A.2):

$$H_{\sigma,\mathrm{R}}|\psi_{\sigma,\mathrm{R}}\rangle + \tau_{\sigma,\mathrm{R}}|\psi_{\sigma,\mathrm{C}}\rangle = E|\psi_{\sigma,\mathrm{R}}\rangle \tag{A.4}$$

$$(E - H_{\sigma,\mathrm{R}})|\psi_{\sigma,\mathrm{R}}\rangle = \tau_{\sigma,\mathrm{R}}|\psi_{\sigma,\mathrm{C}}\rangle \tag{A.5}$$

$$|\psi_{\sigma,\mathrm{R}}\rangle = g_{\sigma,\mathrm{R}}(E)\tau_{\sigma,\mathrm{R}}|\psi_{\sigma,\mathrm{C}}\rangle \tag{A.6}$$

where $g_{\sigma,\mathrm{R}}$ is the surface Green's function of the isolated lead R $[(E - H_{\sigma,\mathrm{R}})g_{\sigma,\mathrm{R}} = I]$.

It is usually easier to calculate the Green's function than solve the whole eigenvalue problem. E.g., the wavefunction of the right lead $(|\psi_{\sigma,\mathrm{R}}\rangle)$ can be calculated if I know the wavefunction on the scattering region $(|\psi_{\sigma,\mathrm{C}}\rangle)$.

A.2 Self-Energy and Transmission

The reason for calculating the Green's function is that it is easier that solving the Schrödinger equation. Also, the Green's function of the central region $(G_{\sigma,\mathrm{C}})$ can be calculated separately without calculating the whole Green's function (G). From the definition of the Green's function I obtain:

$$\begin{pmatrix} E-H_{\sigma,\mathrm{L}} & -\tau_{\sigma,\mathrm{L}} & 0 \\ -\tau^{\dagger}_{\sigma,\mathrm{L}} & E-H_{\sigma,\mathrm{C}} & -\tau^{\dagger}_{\sigma,\mathrm{R}} \\ 0 & -\tau_{\sigma,\mathrm{R}} & E-H_{\sigma,\mathrm{R}} \end{pmatrix} \begin{pmatrix} G_{\sigma,\mathrm{L}} & G_{\sigma,\mathrm{LC}} & G_{\sigma,\mathrm{LR}} \\ G_{\sigma,\mathrm{CL}} & G_{\sigma,\mathrm{C}} & G_{\sigma,\mathrm{CR}} \\ G_{\sigma,\mathrm{RL}} & G_{\sigma,\mathrm{RC}} & G_{\sigma,\mathrm{R}} \end{pmatrix} = \begin{pmatrix} I & 0 & 0 \\ 0 & I & 0 \\ 0 & 0 & I \end{pmatrix} \quad \text{(A.7)}$$

Selecting the three equations in the second column:

$$(E-H_{\sigma,\mathrm{L}})G_{\sigma,\mathrm{LC}} - \tau_{\sigma,\mathrm{L}}G_{\sigma,\mathrm{C}} = 0 \quad \text{(A.8)}$$

$$-\tau^{\dagger}_{\sigma,\mathrm{L}}G_{\sigma,\mathrm{LC}} + (E-H_{\sigma,\mathrm{C}})G_{\sigma,\mathrm{C}} - \tau^{\dagger}_{\sigma,\mathrm{R}}G_{\sigma,\mathrm{RC}} = I \quad \text{(A.9)}$$

$$(E-H_{\sigma,\mathrm{R}})G_{\sigma,\mathrm{RC}} - \tau_{\sigma,\mathrm{R}}G_{\sigma,\mathrm{C}} = 0 \quad \text{(A.10)}$$

I can solve equations (A.8) and (A.10) for $G_{\sigma,\mathrm{LC}}$ and $G_{\sigma,\mathrm{RC}}$:

$$G_{\sigma,\mathrm{LC}} = g_{\sigma,\mathrm{L}}\tau_{\sigma,\mathrm{L}}G_{\sigma,\mathrm{C}} \quad \text{(A.11)}$$

$$G_{\sigma,\mathrm{RC}} = g_{\sigma,\mathrm{R}}\tau_{\sigma,\mathrm{R}}G_{\sigma,\mathrm{C}} \quad \text{(A.12)}$$

substitution into equation (A.9) gives:

$$-\tau^{\dagger}_{\sigma,\mathrm{L}}g_{\sigma,\mathrm{L}}\tau_{\sigma,\mathrm{L}}G_{\sigma,\mathrm{C}} + (E-H_{\sigma,\mathrm{C}})G_{\sigma,\mathrm{C}} - \tau^{\dagger}_{\sigma,\mathrm{R}}g_{\sigma,\mathrm{R}}\tau_{\sigma,\mathrm{R}}G_{\sigma,\mathrm{C}} = I \quad \text{(A.13)}$$

from which $G_{\sigma,\mathrm{C}}$ is simple to find:

$$G_{\sigma,\mathrm{C}} = (E - H_{\sigma,\mathrm{C}} - \Sigma_{\sigma,\mathrm{L}} - \Sigma_{\sigma,\mathrm{R}})^{-1} \quad \text{(A.14)}$$

where $\Sigma_{\sigma,\mathrm{L}} = \tau^{\dagger}_{\sigma,\mathrm{L}}g_{\sigma,\mathrm{L}}\tau_{\sigma,\mathrm{L}}$ and $\Sigma_{\sigma,\mathrm{R}} = \tau^{\dagger}_{\sigma,\mathrm{R}}g_{\sigma,\mathrm{R}}\tau_{\sigma,\mathrm{R}}$ are the so called self-energies.

Loosely one can say that the effect of the leads on the central region is to add the self-energies to the Hamiltonian of the central region since when I calculate the Green's function on the central region I just calculate the Green's function for the effective Hamiltonian $H_{\mathrm{eff}} =$

$H_{\rm C} + \Sigma_{\rm L} + \Sigma_{\rm R}$. However, I should keep in mind that I can only do this when I calculate the Green's function. The eigen-values and -vectors of this effective Hamiltonian are not quantities I can interpret easily.

The transmission is evaluated by the Landauer formula for the noninteracting central region connected with two leads

$$T_\sigma(E) = {\rm Tr}(G^\dagger_{\sigma,{\rm C}}\Gamma_{\sigma,{\rm R}}G_{\sigma,{\rm C}}\Gamma_{\sigma,{\rm L}}) \tag{A.15}$$

where the $\Gamma_{\sigma,{\rm L,R}} = i\left(\Sigma_{\sigma,{\rm L,R}} - \Sigma^\dagger_{\sigma,{\rm L,R}}\right)$.

A.3 Noncollinear spin transmission

Noncollinear density functional theory is based on a two component spinor wave function defined by

$$|\psi_\nu\rangle = \left|\varphi^\uparrow_\nu\uparrow\right\rangle + \left|\varphi^\downarrow_\nu\downarrow\right\rangle \tag{A.16}$$

where $\left|\varphi^\uparrow_\nu\uparrow\right\rangle \equiv \left|\varphi^\uparrow_\nu\right\rangle|\uparrow\rangle$ with a spatial function $\left|\varphi^\uparrow_\nu\right\rangle$ and a spin function $|\uparrow\rangle$. In the noncollinear density functional theory, I solve the two component Kohn-Sham equation as follows:

$$\begin{pmatrix} \hat{T} + w_{\uparrow\uparrow} + V_{\rm H} + V^{\uparrow\uparrow}_{\rm xc} & w_{\uparrow\downarrow} + V^{\uparrow\downarrow}_{\rm xc} \\ w_{\downarrow\uparrow} + V^{\downarrow\uparrow}_{\rm xc} & \hat{T} + w_{\downarrow\downarrow} + V_{\rm H} + V^{\downarrow\downarrow}_{\rm xc} \end{pmatrix} \begin{pmatrix} \varphi^\uparrow_\mu \\ \varphi^\downarrow_\mu \end{pmatrix} = \varepsilon_\mu \begin{pmatrix} \varphi^\uparrow_\mu \\ \varphi^\downarrow_\mu \end{pmatrix}. \tag{A.17}$$

Thus, the expansion from the collinear to noncollinear systems is corresponding to the expansion from one component Hamiltonian to two component Hamiltonian as follows:

$$H_{\uparrow,\downarrow} \Rightarrow \begin{pmatrix} H_{\uparrow\uparrow} & H_{\uparrow\downarrow} \\ H_{\downarrow\uparrow} & H_{\downarrow\downarrow} \end{pmatrix}. \tag{A.18}$$

Therefore, the equation (A.2) is rewritten by

$$\begin{pmatrix} H_{\uparrow\uparrow,{\rm L}} & H_{\uparrow\downarrow,{\rm L}} & \tau_{\uparrow\uparrow,{\rm L}} & \tau_{\uparrow\downarrow,{\rm L}} & 0 & 0 \\ H_{\downarrow\uparrow,{\rm L}} & H_{\downarrow\downarrow,{\rm L}} & \tau_{\downarrow\uparrow,{\rm L}} & \tau_{\downarrow\downarrow,{\rm L}} & 0 & 0 \\ \tau^\dagger_{\uparrow\uparrow,{\rm L}} & \tau^\dagger_{\uparrow\downarrow,{\rm L}} & H_{\uparrow\uparrow,{\rm C}} & H_{\uparrow\downarrow,{\rm C}} & \tau^\dagger_{\uparrow\uparrow,{\rm R}} & \tau^\dagger_{\uparrow\downarrow,{\rm R}} \\ \tau^\dagger_{\downarrow\uparrow,{\rm L}} & \tau^\dagger_{\downarrow\downarrow,{\rm L}} & H_{\downarrow\uparrow,{\rm C}} & H_{\downarrow\downarrow,{\rm C}} & \tau^\dagger_{\downarrow\uparrow,{\rm R}} & \tau^\dagger_{\downarrow\downarrow,{\rm R}} \\ 0 & 0 & \tau_{\uparrow\uparrow,{\rm R}} & \tau_{\uparrow\downarrow,{\rm R}} & H_{\uparrow\uparrow,{\rm R}} & H_{\uparrow\downarrow,{\rm R}} \\ 0 & 0 & \tau_{\downarrow\uparrow,{\rm R}} & \tau_{\downarrow\downarrow,{\rm R}} & H_{\downarrow\uparrow,{\rm R}} & H_{\downarrow\downarrow,{\rm R}} \end{pmatrix} \begin{pmatrix} |\psi_{\uparrow,{\rm L}}\rangle \\ |\psi_{\downarrow,{\rm L}}\rangle \\ |\psi_{\uparrow,{\rm C}}\rangle \\ |\psi_{\downarrow,{\rm C}}\rangle \\ |\psi_{\uparrow,{\rm R}}\rangle \\ |\psi_{\downarrow,{\rm R}}\rangle \end{pmatrix} = E \begin{pmatrix} |\psi_{\uparrow,{\rm L}}\rangle \\ |\psi_{\downarrow,{\rm L}}\rangle \\ |\psi_{\uparrow,{\rm C}}\rangle \\ |\psi_{\downarrow,{\rm C}}\rangle \\ |\psi_{\uparrow,{\rm R}}\rangle \\ |\psi_{\downarrow,{\rm R}}\rangle \end{pmatrix}. \tag{A.19}$$

Hence, the two component surface Green's function, self-energy, and Green's function of the central region are derived from equation (A.19). Finally, double value of the collinear transmission vanished spin index is obtained.

A.4 Test calculation: Zigzag graphene nanoribbon

By using the EGF method within the noncollinear magnetism, I have performed the test calculation of the ZGNR. Figure A.2 shows the configuration of the ZGNR treated by the EGF method within the noncollinear magnetism. In my previous study[52], I found that as θ increased from 0 to 180°, the band gap increased and the total energy decreased as shown in Fig A.3. Because the transmission has to be consistent with the electron number estimated by analysis of the band structure, I calculated the transmission and compared that with the electron number estimated by analysis of the band structure.

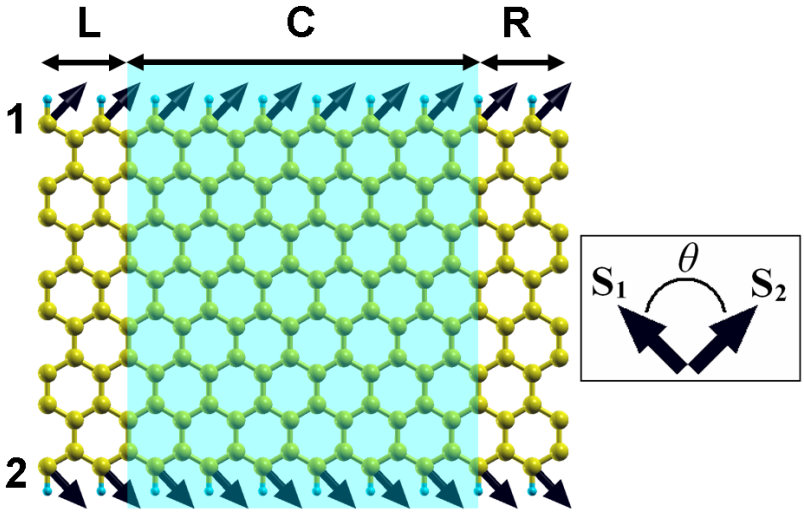

Figure A.2: Configuration of the ZGNR treated by EGF method within the noncollinear magnetism. The yellow and light blue spheres denote C and H atoms, respectively. TThe black arrows denote the magnetic moments S_1 and S_2 at the two edges. The relative angle between S_1 and S_2 is represented by θ. L, C, R means the left and right leads, and the central region, respectively.

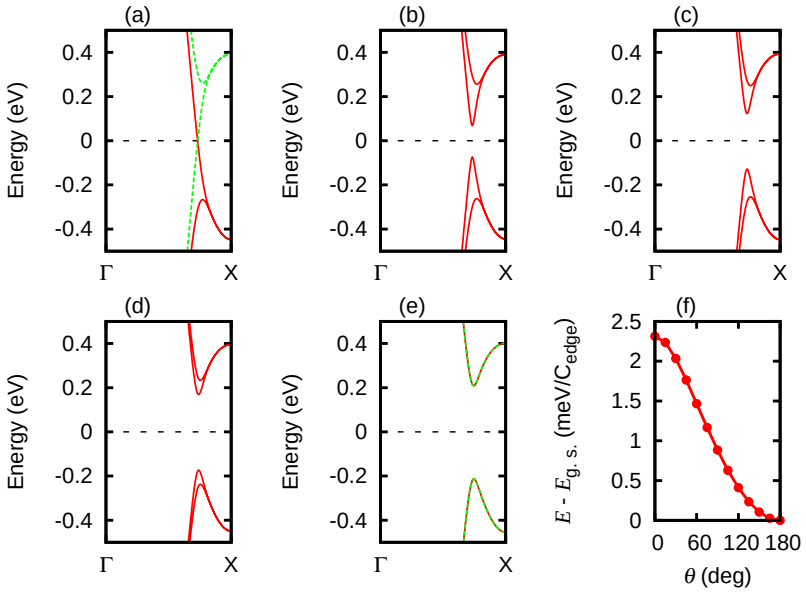

Figure A.3: Band structures of the collinear and noncollinear magnetic (NCM) states in the 10-ZGNR. The solid and dashed lines denote the up and down spin states, respectively, and the Fermi level is located at $E_{\rm F} = 0$. The band structures of PIES (0°), NCM (45°), NCM (90°), NCM (135°), and APIES (180°) states are shown in (a), (b), (c), (d), and (e), respectively. The total energy per edge atom as a function of θ is shown in (f), where the energy is measured from that of the APIES state.

Figure A.4 shows the θ dependence of the transmission in the ZGNR. The transmission gap increases with increasing θ. The tendency of transmission gap is consistent with that of the band gap (Fig. A.3). Therefore, the test calculation used the EGF method within the noncollinear magnetism is successful.

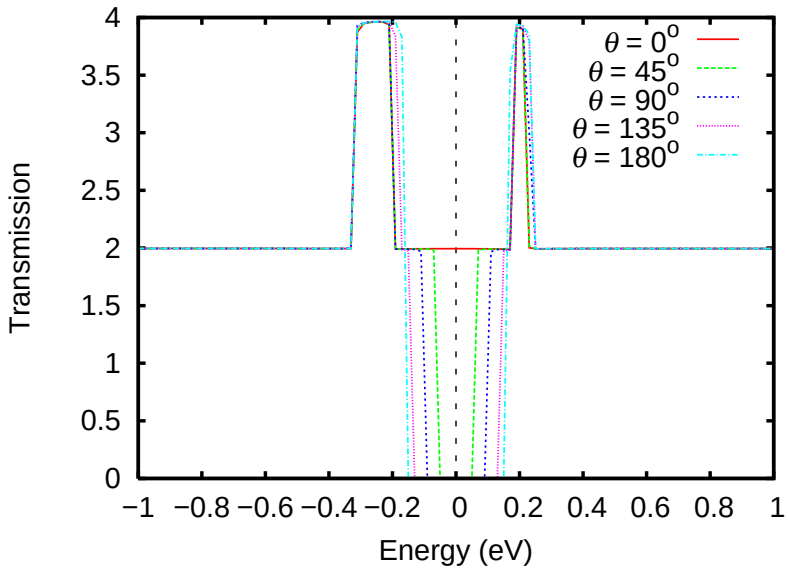

Figure A.4: θ dependence of transmission in ZGNR. The Fermi level is located at $E_{\mathrm{F}} = 0$. The red, green, blue, pink, and light blue lines denote PIES (0°), NCM (45°), NCM (90°), NCM (135°), and APIES (180°) states, respectively.

References

[1] N. Hamada, S. Sawada, and A. Oshiyama, Phys. Rev. Lett. **68**, 1579 (1992)

[2] Y. -W. Son, M. L. Cohen, and S. G. Louie, Nature **444**, 347 (2006)

[3] O. Hod, V. Barone, and G. E. Scuseria, Phya. Rev. B **77**, 035411 (2008)

[4] E. Kan, Z. Li, J. Yang, and J. G. Hou, J. Am. Chem. Soc. **130**, 4224 (2008)

[5] A. F. Hebard, M. J. Rosseinsky, R. C. Haddon, D. W. Murphy, S. H. Glarum, T. T. M. Palstra, A. P. Ramirez, and A. R. Kortan, Nature **350**, 600 (1991)

[6] K. Tanigaki, T. W. Ebbesen, S. Saito, J. Mizuki, J. S. Tsai, Y. Kubo, and S. Kuroshima, Nature **352**, 222 (1991)

[7] P. -M. Allemand, K. C. Khemani, A. Koch, F. Wudl, K. Holczer, S. Donovan, G. Grüner, and J. D. Thompson, Science **253**, 301 (1991)

[8] M. Fujita, K. Wakabayashi, K. Nakada, and K. Kusakabe, J. Phys. Soc. Jpn. **65**, 1920 (1996)

[9] S. Okada, and A. Oshiyama, J. Phys. Soc. Jpn. **72**, 1510 (2003)

[10] K. S. Novoselov, A. K. Geim, S. V. Morozov, D. Jiang, Y. Zhang, S. V. Dubonos, I. V. Grigorieva, and A. A. Firsov, Science **306**, 666 (2004)

[11] M. Ohishi, M. Shiraishi, R. Nouchi, T. Nozaki, T. Shinjo, and Y. Suzuki, Jpn. J. Appl. Phys. **46**, L605 (2007)

[12] N. Tombros, C. Jozsa, M. Popinciuc, H. T. Jonkman, and B. J. van Wees, Nature **448**, 571 (2007)

[13] M. Nishioka, and A. M. Goldman, Appl. Phys. Lett. **90**, 252505 (2007)

[14] J. Bai, R. Cheng, F. Xiu, L. Liao, M. Wang, A. Shailos, K. L. Wang, Y. Huang, and X. Duan, Nature Nanotech. **5**, 655 (2010)

[15] T. Ozaki, K. Nishio, H. Weng, and H. Kino, Phys. Rev. B **81**, 075422 (2010)

[16] D. V. Kosynkin, A. L. Higginbotham, A. Sinitskii, J. R. Lomeda, A. Dimiev, B. K. Price and J. M. Tour, Nature **458**, 872 (2009)

[17] L. Jiao, L. Zhang, X. Wang, G. Diankov and H. Dai, Nature **458**, 877 (2009)

[18] K. Nakada, M. Fujita, G. Dresselhaus, and M. S. Dresselhaus, Phys. Rev. B **54**, 17954 (1996)

[19] S. Okada, and A. Oshiyama, Phys. Rev. Lett. **87**, 146803 (2001)

[20] E. H. Lieb, Phys. Rev. Lett. **62**, 1201 (1989)

[21] K. Kusakabe, and M. Maruyama, Phys. Rev. B **67**, 092406 (2003)

[22] K. Sawada, F. Ishii, M. Saito, S. Okada, and T. Kawai, Nano Lett. **9**, 269 (2009)

[23] Y. Miyamoto, K. Nakada, and M. Fujita, Phys. Rev. B **59**, 9858 (1999)

[24] B. Sahu, H. Min, A. H. MacDonald, and S. K. Banerjee, Phys. Rev. B **78**, 045404 (2008)

[25] B. Sahu, H. Min, and S. K. Banerjee, Phys. Rev. B **81**, 045414 (2010)

[26] B. Sahu, H. Min, and S. K. Banerjee, Phys. Rev. B **82**, 115426 (2010)

[27] G. Kim, and S. -H. Jhi, Appl. Phys. Lett. **97**, 263114 (2010)

[28] G. Bertoni, L. Calmels, A. Altibelli, and V. Serin, Phys. Rev. B **71**, 075402 (2004)

[29] D. Eom, D. Prezzi, K. T. Rim, H. Zhou, M. Lefenfeld, S. Xiao, C. Nuckolls, M. S. Hybertsen, T. F. Heinz, and G. W. Flynn, Nano Lett. **9**, 2844 (2009)

[30] P. Sutter, M. S. Hybertsen, J. T. Sadowski, and E. Sutter, Nano Lett. **9**, 2654 (2009)

[31] J. Coraux, A. T. N‘ Diaye, C. Busse, and T. Michely, Nano Lett. **8**, 565 (2008)

[32] F. Varchon, R. Feng, J. Hass, X. Li, B. N. Nguyen, C. Naud, P. Mallet, J.-Y. Veuillen, C. Berger, E. H. Conrad, and L. Magaud, Phys. Rev. Lett. **99**, 126805 (2007)

[33] M. Ishigami, J. H. Chen, W. G. Cullen, M. S. Fuhrer, and E. D. Williams, Nano Lett. **7**, 1643 (2007)

[34] Y. Gamo, A. Nagashima, M. Wakabayashi, M. Terai, and C. Oshima, Surf. Sci. **374**, 61 (1997)

[35] P. A. Khomyakov, G. Giovannetti, P. C. Rusu, G. Brocks, J. van den Brink, and P. J. Kelly, Phys. Rev. B **79**, 195425 (2009)

[36] S. Okada, Phys. Rev. B **77**, 041408(R) (2008)

[37] Y. Kobayashi, K. Fukui, T. Enoki, K. Kusakabe, and Y. Kaburagi, Phys. Rev. B **71**, 193406 (2005)

[38] H. Lin, T. Hikihara, H. Jeng, B. Huang, C. Mou, and X. Hu, Phys. Rev. B **79**, 035405 (2009)

[39] T. Satoko, and S. Ohnishi,『密度汎関数法とその応用 分子・クラスターの電子状態』, kodansha (1994)

[40] J. P. Perdew, K. Burke, and M. Ernzerhof, Phys. Rev. Lett. **77**, 3865 (1996)

[41] A. Ueda,『Molecular Simulation － from Classical to Quantum Methods －』, shokabo (2003)

[42] T. Ozaki, Phys. Rev. B **67**, 155108 (2003)

[43] T. Ozaki, H. Kino, J. Yu, M. J. Han, N. Kobayashi, M. Ohfuti, F. Ishii, T. Ohwaki, H. Weng, and K. Terakura, http://www.openmx-square.org/

[44] A. D. Becke, and R. M. Dickson, J. Chem. Phys. **89**, 2993 (1988)

[45] N. Troullier, and J. L. Martins, Phys. Rev. B **43**, 1993 (1991)

[46] T. Ozaki, Phys. Rev. B **67**, 155108 (2003)

[47] T. Ozaki, and H. Kino, Phys. Rev. B **69**, 195113 (2004)

[48] S. G. Louie, S. Froyen, and M. L. Cohen, Phys. Rev. B **26**, 1738 (1982)

[49] P. A. Khomyakov, G. Giovannetti, P. C. Rusu, G. Brocks, J. van den Brink, and P. J. Kelly, Phys. Rev. B **79**, 195425 (2009)

[50] T. Kawai, Y. Miyamoto, O. Sugino, and Y. Koga, Phys. Rev. B **62**, R16349 (2000)

[51] L. R. Radovic, and B. Bockrath, J. Am. Chem. Soc. **127**, 5917 (2005)

[52] K. Sawada, F. Ishii, and M. Saito, Appl. Phys. Express **1**, 064004 (2008)

[53] Y. -W. Son, M. L. Cohen, and S. G. Louie, Phys. Rev. Lett. **97**, 216803 (2006)

[54] K. McGuire, N. Gothard, P. L. Gai, M. S. Dresselhaus, G. Sumanasekera, and A. M. Rao, Carbon **43**, 219 (2005)

[55] N. Murata, J. Haruyama, J. Reppert, A. M. Rao, T. Koretsune, S. Saito, M. Matsudaira, and Y. Yagi, Phys. Rev. Lett. **101**, 027002 (2008)

[56] X. Wang, X. Li, L. Zhang, Y. Yoon, P. K. Weber, H. Wang, J. Guo, and H. Dai, Science **324**, 768 (2009)

[57] Y. Lee, S. Kim, and D. Tomanek, Phys. Rev. Lett. **78**, 2393 (1997)

[58] V. A. Rigo, T. B. Martins, Antonio J. R. da Silva, A. Fazzio, and R. H. Miwa, Phys. Rev. B **79**, 075435 (2009)

[59] Z. Zanolli, G. Onida, and J.-C. Charlier, ACS Nano **4**, 5174 (2010)

[60] K. von Bergmann, S. Heinze, M. Bode, E. Y. Vedmedenko, G. Bihlmayer, S. Blügel and R. Wiesendanger, Phys. Rev. Lett. **96**, 167203 (2006)

[61] M. Paulsson, arXiv:cond-mat/0210519 (unpublished)

[62] T. Ozaki, K. Nishio, and H, Kino, Phys. Rev. B **81**, 035116 (2010)

Acknowledgments

I would like to thank my advisors, Prof. Saito and Dr. Ishii (Kanazawa Univ.) for kind encouragement and useful advices for this work. I also would greatly appreciate advices from Prof. Oda, Prof. Miura (Kanazawa Univ.), and Prof. Takasu (Tokyo Univ. of Pharmacy and life sicneces). I am also indebted to Prof. Ozaki (JAIST), Prof. Okada (Tsukuba Univ.), and Dr. Kawai (NEC Corporation) whose meticulous comments were an enoumous help to me. I acknowledge the JSPS for financail support (Grant No. 21-2252). I would also like to express my gratitude to my family for their moral support and warm encouragements.